

Attention towards chemistry agnostic and explainable battery lifetime prediction

Fuzhan Rahmanian^{1,2,4,5,6*}, Robert M. Lee³, Dominik Linzner³, Kathrin Michel³, Leon Merker^{1,2}, Balazs B. Berkes³, Leah Nuss^{1,4,5,6}, and Helge Sören Stein^{4,5,6*}

¹Helmholtz Institute Ulm, Applied Electrochemistry, Helmholtzstr. 11, 89081 Ulm, Germany

²Karlsruhe Institute of Technology, Institute of Physical Chemistry, Fritz-Haber-Weg 2, 76131 Karlsruhe, Germany

³BASF SE, Ludwigshafen, Germany

⁴Technische Universität München, School of Natural Sciences, Department of Chemistry Lichtenbergstr 4, 85748 Garching, Germany

⁵Technische Universität München, Munich Data Science Institute, Walther-von-Dyck-Straße 10, 4, 85748 Garching, Germany

⁶Technische Universität München, Munich Institute for Robotic and Machine Intelligence, Georg-Brauchle-Ring 60-62, 80992 Munich, Germany

*corresponding author(s): Helge Sören Stein (helge.stein@tum.de), Fuzhan Rahmanian (fuzhan.rahmanian@tum.de)

Abstract

Predicting and monitoring battery life early and across chemistries is a significant challenge due to the plethora of degradation paths, form factors, and electrochemical testing protocols. Existing models typically translate poorly across different electrode, electrolyte, and additive materials, mostly require a fixed number of cycles, and are limited to a single discharge protocol. Here, an attention-based recurrent algorithm for neural analysis (ARCANA) architecture is developed and trained on a unique, ultra-large, proprietary dataset from BASF and a large Li-ion dataset gathered from literature across the globe. ARCANA generalizes well across this diverse set of chemistries, electrolyte formulations, battery designs, and cycling protocols and thus allows for universal extraction of data-driven knowledge of the degradation mechanisms. The model's adaptability is further demonstrated through fine-tuning on Na-ion batteries. ARCANA advances the frontier of large-scale time series models in analytical chemistry beyond textual data and holds the potential to significantly accelerate discovery-oriented battery research endeavors.

1 Introduction

Lithium-ion batteries (LIBs) enable the electrification of everything, yet there is a maze of challenges that must be navigated in order to optimize the batteries of the future ^{5, 61, 51, 15}. Critical to the advancement of battery research is the rapid understanding of why and how some batteries degrade and what needs to be changed to prevent premature capacity fade ⁵⁴. Material degradation can occur due to numerous factors, including unpreventable solid electrolyte interphase growth, loss of active material, and other electrochemical phenomena ³¹. However, investigating battery degradation is a time-consuming task, as non-linear capacity loss can occur over hundreds or thousands of cycles ⁶. Another challenge in early lifetime prediction is the diversity of battery chemistries in the anode, cathode, and electrolyte, along with various form factors and testing protocols.

Battery lifetime can be evaluated through various methods, such as conventional cycling until end of life (EOL) under constant current-constant voltage (CC-CV) conditions or cycling for a predetermined

42 number of cycles. From these data, measures such as coulombic efficiency (CE) can be calculated ⁶²
43 and correlated to more in-depth techniques such as electrochemical impedance spectroscopy (EIS) ⁴⁶ to
44 fundamentally assess the underlying degradation mechanisms. Accurate measurement of CE ^{18, 52} does,
45 however, require bespoke instrumentation and a considerable amount of time, i.e. cycling a battery
46 for 1000 cycles at $1C/1D$ takes approximately 11 weeks. Reducing the required number of cycles
47 by a factor of 10, while maintaining a high level of fidelity, is therefore of great interest ⁷. Machine
48 Learning (ML) and Deep Learning (DL) can accelerate testing by lowering the number of cycles
49 required to understand the underlying chemistries ³. An example of predicting EOL of batteries using
50 initial discharge capacity curves was demonstrated by Severson et al. ⁵¹, who used regression models.
51 They integrated data generation with data-driven models to forecast the lifetime of LFP/graphite cells
52 based on $\Delta Q(V)$ and classified their longevity. In further work, Attia et al. ⁷ employed a Bayesian
53 algorithm to accelerate the optimization of fast-charging protocols. By using early-cycle data for low-
54 fidelity predictions, the approach enabled the optimization of high-fidelity experimental outcomes, thus
55 significantly reducing the experimental duration from 500 to 16 days.

56 The most reliable models do not, however, merely predict just predict a quantity but also allow as-
57 sessment of the model's uncertainty. Emblematic of this is the work by Tong et al. ⁵⁶, who introduced
58 ADLSTM-MC, a hybrid predictive model using adaptive dropout long short term memory (LSTM)
59 with Monte Carlo simulations. This approach, which requires minimal training data, enhances robust-
60 ness through Bayesian-optimized dropout rates and improves the remaining useful life of two types
61 of LIBs. In a correlative study ⁴⁷, a recurrent autoregressive deep ensemble network with aleatoric
62 and epistemic uncertainties was developed along with saliency analysis to assess the impact of input
63 parameters on output prediction. This provided an intuitive understanding of feature importance.
64 Another advantage of using DL algorithms is their ability to use raw data, which has gained interest in
65 the estimation of battery State of Health (SOH). For instance, Yang et al. ⁶³ developed a novel hybrid
66 convolutional neural network architecture with parallel residual connections, which utilizes raw data
67 across multiple dimensions. By incorporating attention mechanisms, their model achieves remarkable
68 accuracy in predicting the early stages of degradation. Although these approaches are applied in bat-
69 tery research ^{27, 68}, their prominence is not as widespread as in other scientific fields. However, this
70 lesser emphasis provides an opportunity for further exploration and discovery. Beyond these early life-
71 time prediction models, sequence-to-sequence (Seq-to-Seq) models have been used to monitor battery
72 lifetime and SOH ^{27, 34, 20}. They leverage intrinsic temporal dependencies in degradation data, provid-
73 ing high predictive accuracy and computational efficiency. Li et al. ³⁴ developed a one-shot LSTM-based
74 Seq-to-Seq framework which not only predicts future capacities, but also identifies knee points in the
75 degradation curve, maintaining stability even in the face of stochastic disturbances. Although Seq-to-
76 Seq models demonstrate robust predictions, they also exhibit limitations in generalization and require
77 large and diverse datasets to enhance performance ¹⁵.

78 Despite the promises made by ML and DL for lifetime predictions ^{11, 24, 55}, these models, while
79 robust, face challenges of precision and trustworthiness ³⁶. Existing models often focus on single-task
80 learning, neglecting the potential benefits of multi-objective learning for various predictive settings ¹⁵.
81 In particular, data-driven approaches ⁴⁰ tend to overlook the inherent variations between, for ex-
82 ample, production batches or individual cells ⁹. Such discrepancies, originating from manufacturing
83 processes or aging mechanisms, can profoundly impact lifetime predictions. Addressing these varia-
84 tions for accurate forecasting remains a central yet unresolved research question. Furthermore, despite
85 the assertions of recent studies that they are chemistry-agnostic ^{47, 48}, they often require enhanced
86 explainability to optimize their effectiveness in various chemistry settings. Transfer learning offers a
87 promising solution to the challenge of scarce data, but requires more investigation for transparency
88 and interpretability ³⁰. The acquisition of extensive datasets, essential for DL algorithms ⁶⁴, remains a
89 significant hurdle ^{22, 40, 59}. Nevertheless, innovative strategies, such as the use of common features in
90 databases and the documentation of various chemistries and protocols ³⁵, establish the foundation for
91 more in-depth research ⁶⁴. Our goal is to develop a model that is not only universally applicable, but
92 also robust, with the capability to provide both uncertainty quantification and explainability. Such a
93 model would be invaluable to the academic community and would find marketable applications in the
94 real world ⁶⁴, accelerating battery design and data collection based on active learning.

2 Results

2.1 Data resources

Developing a model that generalizes well necessitates a diverse and large dataset⁴⁰ that ideally covers a spectrum of chemistries and formats given high-dimensional correlations and cell variations^{66, 30}, obtained from various laboratories and measured under different operating conditions⁷. Data diversity not only ensures an accurate representation of different cycling behaviors, but also tames the irreducible uncertainty in the predictions while mitigating the risk of overfitting. However, the scarcity of large and comprehensive datasets³⁶ that include both high and low-performing cells creates a challenge for training generalized models, i.e., to overcome a positive bias^{45, 30}. Available data often exhibit noise, discontinuities, and varying formats that require extensive curation, adding a layer of complexity. Initiatives such as Battery Archive¹⁹ or other cloud services³² are therefore commendable in promoting Findable, Accessible, Interoperable, and Reusable (FAIR) data^{23, 58} handling in battery research^{22, 59}.

In this study, we develop a model trained on ca. 17400 batteries from BASF research laboratories that covers a diverse range of LIBs chemistries and multiple cycling protocols. Exposure of our model to such a wide variety of data enables robust generalization. Utilizing our pre-trained model on a unique set of unseen data, we effectively predict the early degradation trajectory. The ultimate test of our model, therefore, is to apply it to data from cells produced in a different location and with varying chemistries. Due to intellectual property constraints that prevent the authors from making the model trained on the BASF dataset openly accessible, we have retrained our model by leveraging a diverse array of publicly available datasets from respected institutions and research groups, including the Toyota Research Institute (TRI) in partnership with MIT and Stanford^{2, 1}, NASA⁵⁰, the Center for Advanced Life Cycle Engineering (CALCE)²⁹, Karlsruhe Institute of Technology (KIT)⁶⁹, Hawaii Natural Energy Institute (HNEI)²¹, and Sandia National Laboratories (SNL)²¹. Furthermore, we have incorporated data from our in-house cycled cells^{67, 38, 39, 42} with successful and failed experiments, to further enrich model training and reduce bias. In the Supplementary Section 1 we provide an overview of all datasets; we include a brief summary in table 1 with an indication of which datasets were used during training and which remained completely unseen for model testing. This approach ensures a thorough understanding of the data sources, thus improving the transparency and reproducibility of our research.

2.2 Architecture Overview

Central to this study is the Attention-based ReCurrent Algorithm for Neural Analysis with LSTM (ARCANA) model. This is an attention-based Seq-to-Seq architecture specifically engineered to assess early stage battery degradation and perform lifecycle monitoring. The model demonstrates superior multitasking capabilities, supported by its high modularity and dynamic adaptability. It is designed to utilize a flexible range of past battery cycle data, known as historical temporal segments, for input. In addition, the model includes predetermined parameters for future conditions, such as discharge rates and cycle numbers. These parameters are known in advance of the experiment, i.e. they are controlled by the measurement device and are referred to as encoded temporal segments. This dual capability offers multifaceted advantages, from cost and time savings to improved material selection and protocol optimization.

The ARCANA model is augmented with additional features such as the attention mechanism, which provides insight into the decision-making process of the model. This feature distinguishes between predictions based on underlying patterns and those arising from stochastic variability. Saliency analysis is additionally performed to emphasize the relative importance of each parameter through a computation of the absolute gradient of the model output relative to the input of the test set. It quantifies the sensitivity of the input parameters, revealing how minor variations significantly alter the output results⁴⁷, thus aligning the internal logic of the model with domain-specific knowledge. Adding another layer of robustness is uncertainty quantification, which is valuable not only for understanding the reliability of cycling protocols, but also for assessing material performance across different battery chemistries.

As illustrated in the Unified Modeling Language (UML) diagram (Fig. 1), the ARCANA model consists of four principal classes, each performing a different function, and is designed to accept raw data, thus negating the need for preliminary feature engineering. This design versatility extends to its operational modes with Naive Training for initial experiments, Dynamic Tuning for real-time

Table 1: An overview of the collected cycling data utilized for training and testing. The model $M(B)$, was trained with data provided by BASF, and the model $M(P)$ was trained with publicly available data. The model $M(P)_f$ represents a fine-tuned version of $M(P)$ for lithium-ion coin cell data. $M(P)_{Na}$ and $M(B)_{Na}$ models are fine-tuned $M(B)$ and $M(P)$, respectively, adapted for sodium coin cells.

Location	Cell form	Cell chemistry	Protocol Charge\Discharge	No. Cell	Cycle range	Nominal capacity [Ah]	Usage
BASF	Coin	heterogenous	multimodal	17400	multimodal	multimodal	$M(B)$ Train\Val
TRI ²	Cylindrical commercial	LFP\graphite	$CC1(Q1)CC2$, $CC - CV@1C, 4.2V$ \CC@4C	124	169 – 2235	1.1	$M(P)$ Train\Val
TRI ¹	Cylindrical commercial	LFP\graphite	$CC1(20\%)CC2(40\%)$ $CC3(60\%)CC4(80\%)$, $CC - CV@1C, 4.2V$ \CC - CV@4C, 2V	233	100 – 862	1.1	$M(P)$ Train\Val
CALCE ²⁹	Prismatic commercial CX2	LCO\graphite	$CC - CV@0.5C, 4.2V$, 6 \CC@(0.5C, 1C)		781 – 1082	1.35	Testing
CALCE ²⁹	Prismatic commercial CS2	LCO\graphite	$CC - CV@0.5C, 4.2V$, 6 \CC@0.5C		1701 – 2016	1.1	$M(P)$ Train\Val
KIT ⁶⁹	Cylindrical commercial	NCA\graphite-Si	$CC - CV$ @(0.25C, 0.5C, 1C), 4.2V, \CC@1C	58	29 – 800	3.5	$M(P)$ Train\Val
KIT ⁶⁹	Cylindrical commercial	NCM\graphite-Si	$CC - CV$ @(0.25C, 0.5C, 1C), 4.2V, \CC@1C	55	43 – 1277	3.5	$M(P)$ Train\Val
KIT ⁶⁹	Cylindrical commercial	NCM+NCA\graphite	$CC - CV@0.5C, 4.2V$, 9 \CC@(1C, 2C, 4C)		912 – 1031	2.5	Testing
KIT ⁶⁷	Coin self-made	LNO\graphite	$CC - CV@1C, 4.2V$, 43 \CC@1C		82 – 505	0.004618	60% for $M(P)_f$, 40% Testing
KIT ³⁸	Coin commercial	LCO\graphite	$CC - CV@1C, 4.25V$, 26 \CC - CV@1C, 2.75V		150 – 600	0.045	$M(P)$ Train\Val
KIT ³⁹	Coin self-made	NMC622\graphite	$CC - CV@1C, 4.2V$, 11 \CC@1C		228 – 501	0.00328	Testing
KIT ⁴²	Coin self-made	$Na_{0.9}[\dots]O_2$ \graphite	$CC@1C$ \CC@1C or C-rates test	44	40 – 140	0.00015	60% for $M(P)_{Na}$ and $M(B)_{Na}$, 40% Testing
NASA ⁵⁰	Cylindrical commercial	NCA\graphite	$CC - CV$ @0.75C, 4.2V, \CC@(0.5C, 1C, 2C)	34	24 – 196	2.0	$M(P)$ Train\Val
HNEI ²¹	Cylindrical commercial	LCO-NMC\graphite	$CC - CV@0.5C, 4.3V$, 14 \CC@1.5C		1102 – 1133	2.8	$M(P)$ Train\Val
SNL ²¹	Cylindrical commercial	LFP\graphite	$CC - CV$ @0.5C, 4.2V, \CC@(0.5C, 1C, 2C, 3C)	28	2621 – 19174	1.1	$M(P)$ Train\Val
SNL ²¹	Cylindrical commercial	NCA\graphite	$CC - CV$ @0.5C, 4.2V, \CC@(0.5C, 1C, 2C)	24	463 – 7877	3.2	$M(P)$ Train\Val
SNL ²¹	Cylindrical commercial	NMC\graphite	$CC - CV$ @0.5C, 4.2V, \CC@(0.5C, 1C, 2C, 3C)	25	388 – 11149	3.0	$M(P)$ Train\Val

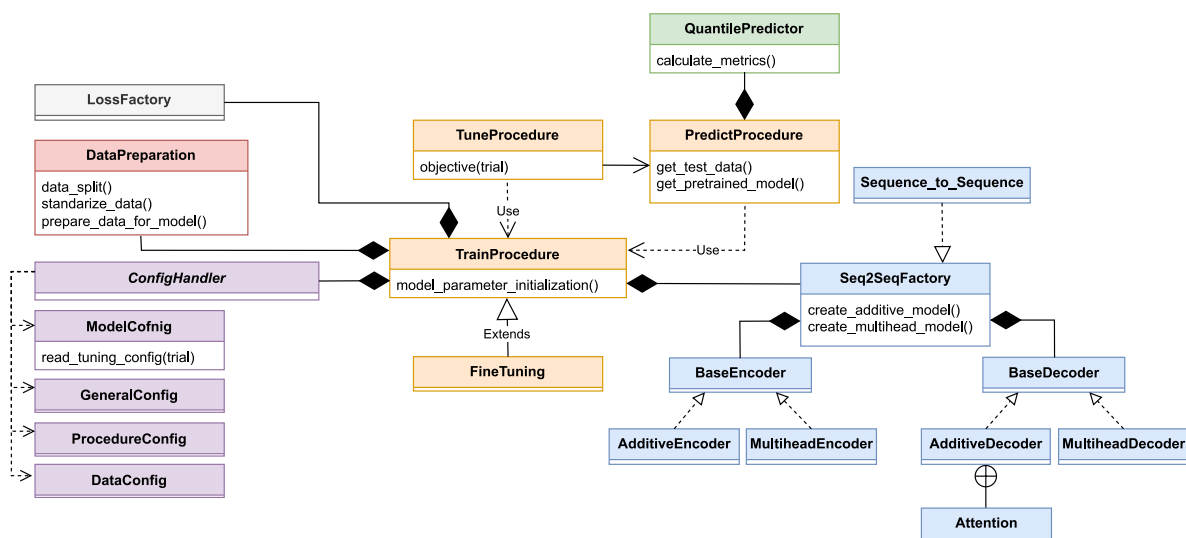


Figure 1: An UML diagram of the computational framework, designed around three principal class clusters. The first includes a `ConfigHandler` engineered to manage a comprehensive set of user-defined configurations and establishes a blueprint for handling various subconfigurations such as general settings, data properties, and model specifications. During hyperparameter optimization tasks, `ConfigHandler` interfaces with the Optuna optimization library to adaptively create and update the tuning configuration. The second key class structure includes `TrainProcedure` which serves as an architectural template for the training process. Its attributes are employed throughout the computational pipeline, starting with data preparation and extending to instantiation of specialized loss functions and Seq2Seq models via the `LossFactory` and `Seq2SeqFactory`. `FineTuning`, is a specialized subclass that inherits from `TrainProcedure` while `TuneProcedure` and `PredictProcedure`, the latter of which uses the `QuantilePredictor`, are incorporated into the pipeline depending on the desired use case and settings. The tuning operates on single trials with a `TPESampler` when multiple runs are desired. Lastly, `Seq2SeqFactory` is engineered to govern the instantiation of encoder-decoder architectures. Depending on the user-defined configurations, it can orchestrate a multihead or an additive encoder-decoder mechanism. The inclusion of custom attention mechanisms within the architecture is handled by the `AdditiveDecoder` class or the `MultiheadDecoder`, conditional upon the configuration stipulations.

150 adaptability via extensive hyperparameter optimization, Fine-Tuning for integration of a pretrained
 151 model with selective gradient updating, and Prediction for efficient inference. Through modularity, a
 152 logging mechanism ensures data integrity and traceability, adhering to FAIR data principles⁵⁸. The
 153 open source codebase uses the PyTorch library⁴³ for model development and the Optuna library⁴ for
 154 hyperparameter optimization.

155 The Encoder-Decoder Framework

156 The encoder (Fig.2a) initiates the Seq-to-Seq model in the ARCANA framework by processing
 157 historical temporal segments of the past battery life cycles. Employing a LSTM network, it is designed
 158 to capture complex, non-linear relationships and time dependencies inherent in sequence data. The
 159 encoder processes the input tensor to accommodate sequences of different lengths, employing a padding
 160 mechanism that enables the LSTM to efficiently process these sequences without being constrained
 161 by their varying lengths. Within the LSTM, the temporal data is transformed into a new tensor,
 162 constructing hidden and cell states that capture sequential information. A skip connection incorporates
 163 the initial input into the LSTM output, thus preserving crucial temporal features and stabilizing
 164 the learning process. Layer normalization, when applied to the LSTM output, not only accelerates
 165 convergence but also leads to robust performance, mitigating the challenges associated with long-
 166 sequence dependencies¹⁷. The encoder returns a rich latent representation of the historical data,
 167 consisting of the output tensor and the updated hidden and cell states, which are then utilized by the
 168 decoder to enable accurate forecasting in subsequent steps.

169 The decoder (Fig. 2a) takes on the task of generating future state predictions. It is initialized with
 170 the hidden and cell states from the encoder and begins by processing the most recent historical cycle
 171 data. The model then integrates its own previous predictions and known future conditions, such as
 172 the expected discharge current and the cycle number. These two inputs are temporally encoded to
 173 capture their positional relevance⁶⁵, ensuring that the decoder is informed of the predefined condition
 174 and the timing of each data point within the life cycle. The decoder employs an attention mechanism
 175 that can dynamically adjust sequence weights, identifying critical information at each prediction step.
 176 This approach overcomes the limitations of static-length vector representation in conventional encoder-

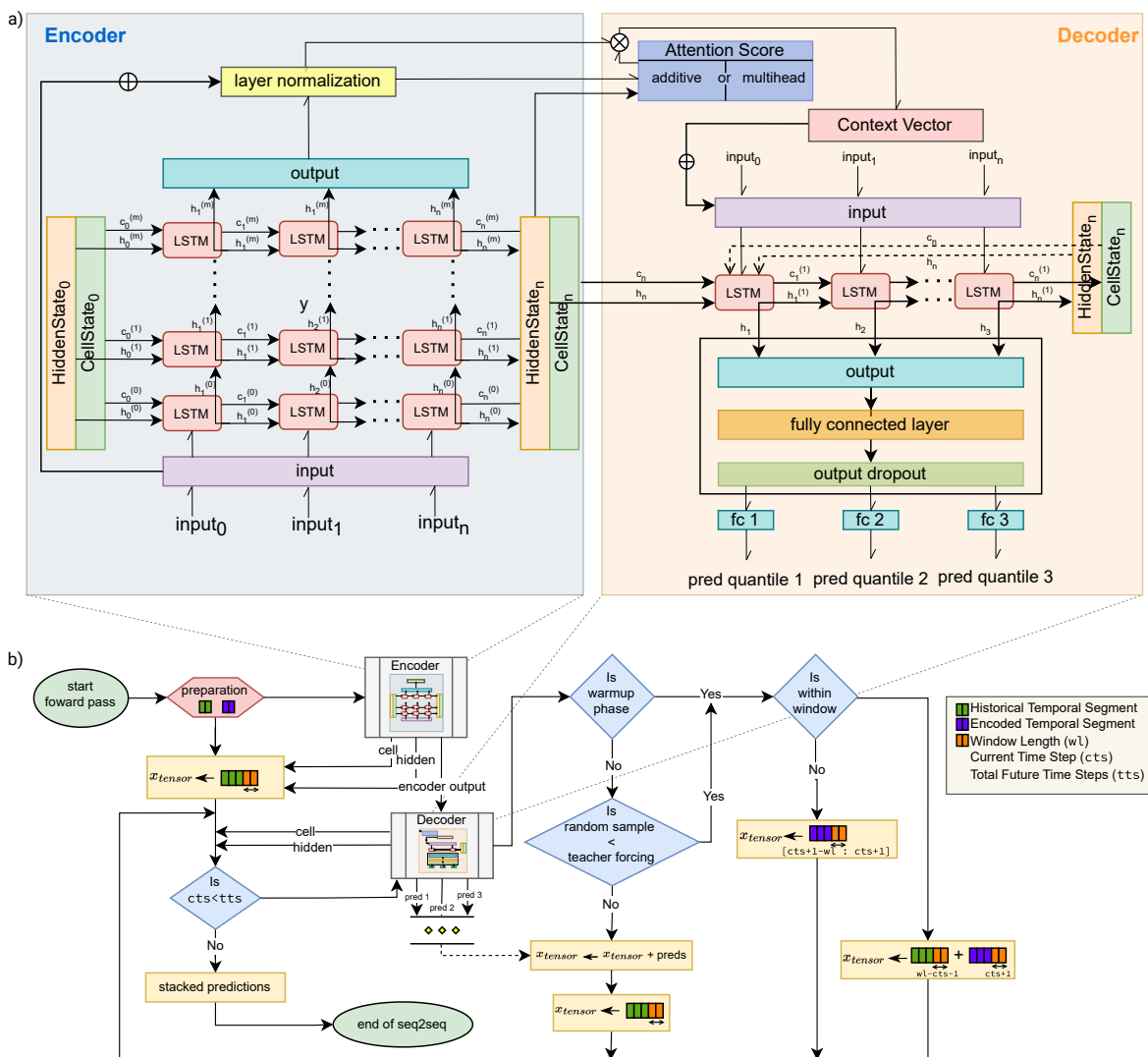


Figure 2: Architectural overview of Seq-to-Seq model. a) Presents the detailed architecture of the encoder and decoder components. The LSTM-based encoder processes historical temporal segments to capture the intricate pattern of battery life cycles. It integrates a skip-connection and layer normalization to preserve and stabilize essential key temporal features. The decoder is initialized with the encoder's final states and applies an attention mechanism to focus on relevant temporal features from the encoder output and enrich the context of its predictions. The attention-enhanced representations are combined with the initial decoder input and subsequently propagated through LSTM layers. A fully connected layer with leaky ReLU activation and a dropout layer - used solely during training and inactive during inference - for regularization, follow the LSTM outputs. The model outputs are then fed into three separate fully connected layers for predicting a specific quantile of the future distribution based on the pattern learned during training, thus providing a probabilistic characterization of the forecast. b) Illustrates the integrated Seq-to-Seq model flow, depicting the progression from encoding historical data to multi-output future forecasts. It highlights the sliding-window approach that underpins the model's capability to handle both the tail-end of historical data and the integration of self-generated forecasts with known future conditions. This process also captures the dynamic training process, which incorporates teacher forcing to enhance the predictive fidelity of the model.

177 decoder models⁸, allowing the decoder to focus on the most relevant parts of historical data. The
178 attention mechanism then computes a context vector associated with the encoder’s output, which
179 highlights the encoder sequences with the highest relevance to the current decoding task. This context
180 vector, combined with the current input, forms a feature-rich tensor that is subsequently processed by a
181 LSTM layer. Post-LSTM, the output layer is passed through a fully connected layer with a leaky ReLU
182 activation function, crucial in maintaining network stability, and enhanced with a dropout layer placed
183 to reduce overfitting risks. The culmination of this process is a decoder that generates forecasts for the
184 0.1, 0.5, and 0.9 quantiles. These provide a probabilistic range indicative of the inherent uncertainty
185 and offer a statistical interpretation of the potential future states of the degradation profile.

186 Seq-to-Seq Integration

187 In the broader Seq-to-Seq model, the encoder and decoder are orchestrated to facilitate the overall
188 predictions, as can be seen in Fig. 2b. Here, the model processes the temporal data using a sliding
189 window approach that enhances the ability to discern local patterns within long input sequences⁶⁵.
190 This technique allows for the integration of the last observed data or transition to the decoder’s self-
191 generated predictions, supplemented with temporally encoded future conditions. During training, a
192 dynamic teacher forcing strategy is employed, in which actual target outputs are used as inputs in
193 lieu of previous predictions to promote model convergence, prediction fidelity, and generalizability
194 in the model. This hybrid training strategy allows effective learning from the ground truth while
195 gradually becoming equipped for self-guided predictions. At the end of the processing of this sequence,
196 quantile-based predictions are collected into a stack of tensors, encapsulating a comprehensive forecast
197 for subsequent decision-making processes. Thus, this forward pass provides fine-grained, probabilistic
198 understanding of the evolving battery life-cycle stages, with the potential to inform risk assessment
199 and optimize operational efficiency.

200 2.3 Experimental configuration

201 This study evaluates the ARCANA architectural model through a two-stage experimental process. Our
202 aim is to present findings that resonate across multiple disciplines, highlighting both the complexity
203 and versatility of our approach. The first stage involved training the model M with the coin cell
204 dataset B from BASF. The resulting trained model is here denoted $M(B)$. We encoded predetermined
205 parameters, including cycle number and discharge current, into temporal segments to capture past
206 and future discharge conditions. The training used an additive attention mechanism in the ARCANA
207 architecture for initial learning, with a detailed explanation in Sec. 4.1. In the second stage, the model
208 M is re-trained from scratch, with publicly available datasets as mentioned in Table. 1, and denoted as
209 $M(P)$. This entails various cell types, including 26 coin cells and 6 prismatic cells with Lithium-Cobalt-
210 Oxide (LCO) cathodes, with the majority being cylindrical cells with Lithium-Iron-Phosphate (LFP),
211 Nickel-Manganese-Cobalt (NMC), and Nickel-Cobalt-Aluminum Oxide (NCA) cathode materials. To
212 address these cell chemistry variations, we introduced an additional predefined parameter, the nominal
213 capacity of each cell in logarithmic format. This inclusion was critical for the model to effectively
214 differentiate and interpret response characteristics⁵³. The public dataset selected for $M(P)$, was
215 significantly smaller, comprising 627 cell entries and accounting for only 3.35% of the total data size
216 of the initial model $M(B)$. The dataset was distributed with 65% for training, 30% for validation, and
217 5% for testing.

218 To emphasize generalizability and test model performance, we incorporated four distinct test
219 datasets, each sourced from different locations and created by various experts. The first two test
220 sets, denoted (D_{LNO}) and D_{NMC} , comprise coin cell measurements made at the Institute of Physical
221 Chemistry (IPC) of KIT, featuring the Lithium-Nickel-Oxide (LNO) and NMC materials, respectively.
222 The third dataset consisted of cylindrical cells from Institute of Applied Materials (IAM) of KIT,
223 containing NMC blended with NCA cathode materials ($D_{NMC+NCA}$). The final dataset involved
224 prismatic cells of the CALCE institute, with LCO materials (D_{LCO}). The complete description of
225 these cells is provided in the Supplementary Section 1. This approach in dataset selection and testing
226 allowed an in-depth evaluation of $M(P)$ for its adaptability to various cell types and experimental
227 setups.

228 The publicly available data for $M(P)$ presented unique challenges as they included prematurely
229 failed cells and high experimental noise, in contrast to the high-quality data used for training $M(B)$.

230 These complexities required a change from an additive to a multihead attention mechanism in $M(P)$.
231 We also encountered a wide range of cycles, from as few as 196 to as many as 19176. However, most of
232 the tests we considered had fewer than 500 cycles. This variability posed a potential risk of gradient
233 instability and inconsistent learning in the training process. To mitigate the risk of poor convergence
234 and the possibility of overfitting, we adopted a standardization approach in which all cells were limited
235 to a maximum of 500 cycles, ensuring better balance in the training data and reducing bias, thus
236 increasing reliability.

237 Both $M(B)$ and $M(P)$ focused on predicting three parameters, which were selected for their estab-
238 lished significance in the existing literature and their availability across the datasets. They included
239 discharge capacity, crucial for understanding the SOH⁵¹, CE, as emphasized in studies by Burns et
240 al.^{13, 14} as the key to understanding the impact of electrode additives and electrode materials on
241 battery long-term performance, and the voltage drop during the relaxation phase between charging
242 and discharging cycles. The last parameter is less explored but, as described by e.g. Zhu et al.⁷⁰, it
243 offers valuable insights independent of the charging process. This parameter is easily calculated from
244 cycling data, even if the studies where the data originated did not directly measure it. In this section,
245 we evaluate our model's performance on various scenarios, focusing on the impact of data quality on
246 model generalization and interpretability, investigating its adaptability to different chemistries, and
247 deriving insights from attention mechanisms and saliency analysis.

248 2.4 Model performance across battery types

249 The hyperparameters of $M(P)$ were selected using Optuna's hyperparameter tuning with 250 trials
250 and are described in the Supp. 3. The model generalization is evaluated on two datasets; cylindrical
251 cells of $D_{NMC+NCA}$ and prismatic cells of D_{LCO} , neither of which were seen by the model during
252 training. Here, the objective was to determine how effectively the model generalizes across different
253 battery configurations despite the presence of noisy data.

254 As shown in Fig. 3, the model handles multidimensional predictions for both $D_{NMC+NCA}$ and
255 D_{LCO} well. For $D_{NMC+NCA}$, it accurately forecasts up to 500 cycles based on 24 input cycles (see
256 Panel I, Fig. 3) even though the extracted data exhibits occasional jumps, despite the discharge
257 current remaining constant throughout. Given that these unexpected jumps are not annotated in the
258 original dataset, we have chosen to acknowledge their presence, but not alter them for the sake of
259 data integrity. Aggregated attention weights in early cycles indicate their importance for long-term
260 forecasting. Emblematic is D_{LCO} , that starts from a 23 cycle profile (Panel II, Fig. 3); the model
261 demonstrates robustness even in the presence of more complex noise patterns. Here, the attention
262 weights are distributed not only in the initial cycles but also in later cycles, proving the necessity of
263 incorporating an attention mechanism.

264 Illustrating the model's generalization capabilities, a detailed analysis of Q_{dis} in Fig. 4 is presented.
265 In both $D_{NMC+NCA}$ and D_{LCO} , there is good agreement between the model's predictions and actual
266 values (Panel I & II, Fig. 4a), as complemented by the density graphs in Fig. 4b. For $D_{NMC+NCA}$, the
267 predicted and actual densities closely overlap. For D_{LCO} , the predicted density is highly similar, with
268 a slightly skewed distribution towards lower Q_{dis} . The better density distributions for $D_{NMC+NCA}$
269 are likely attributable to the larger proportion of cylindrical cells in the training data, which accounts
270 for 94.9% of the total.

271 A detailed evaluation of the uncertainty of the model $M(P)$ is provided in Fig. 4c-e for both
272 datasets. Panel I & II of Fig. 4c evaluate the calibration by comparing the observed quantile proportions
273 to the expected proportions under the assumption of a normal distribution. This continuous curve
274 indicates the model's general performance across the entire probability distribution. The miscalibration
275 area, quantified by the degree of deviation from the ideal diagonal line, represents the aggregate of
276 discrepancies²⁸. For $D_{NMC+NCA}$, the predicted distribution of Q_{dis} is well calibrated around the
277 median but diverges at the tail, with calibration points showing underconfidence at higher quantiles.
278 For D_{LCO} the individual calibration points suggest a slight overconfidence in the 10th-50th percentile
279 and underconfidence in the ranges 50th-90th and 10th-90th percentile. The miscalibration areas for
280 D_{LCO} is 0.16, which is slightly higher than $D_{NMC+NCA}$, likely due to noisier data. The overall
281 calibration performance across both datasets is comparable. Fig. 4 e) shows a histogram of prediction
282 interval quantiles, revealing the spread between the 10th and 90th percentiles and evaluating the
283 concentration of its predictive distribution as indicated by sharpness. The lower values suggest higher
284 confidence in the prediction²⁵. For $D_{NMC+NCA}$, a bimodal distribution highlights variable prediction

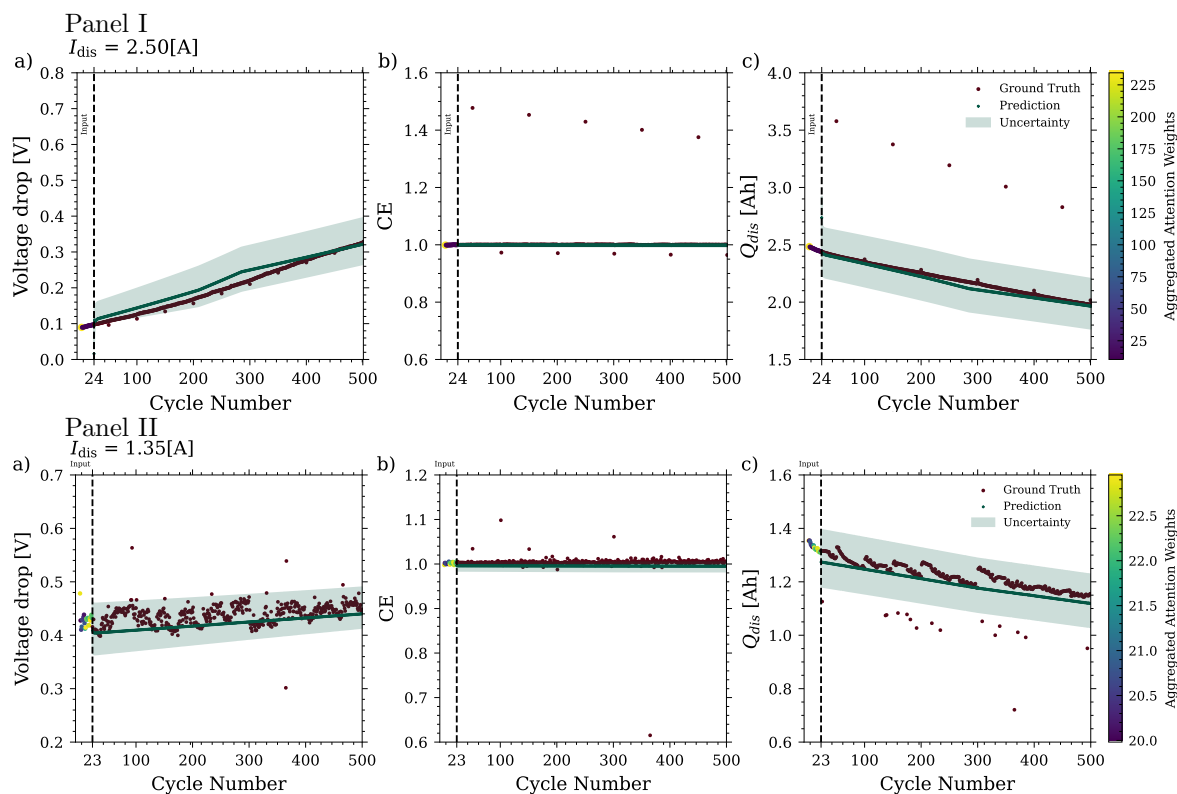


Figure 3: ARCANAs predictive performance on two datasets, namely cylindrical $D_{NMC+NCA}$ in Panel I and prismatic D_{LCO} in Panel II, when predicting battery behaviour over 500 cycles for three predictors of Voltage drop [V], CE and Q_{dis} [Ah]. The model emphasizes its robust noise filtering and adaptive attention mechanism across different data characteristics.

certainty across cycles, suggesting potential fluctuations in battery behavior. D_{LCO} shows two clusters of distributions, mostly around a central quantile with a sharpness of 0.19, indicative of consistent uncertainty. Fig. 4d further supports these findings by illustrating the model's median prediction uncertainty and the variability of these predictions by interquartile range (IQR). Here, $D_{NMC+NCA}$ in Panel I shows varying IQR, suggesting changes in model confidence over lifespan. In contrast, D_{LCO} maintains a more uniform IQR, indicating steady prediction uncertainty and aligning with the model's attention on later cycles to contend with the increased complexity and noise. These metrics complement the information provided in Fig. 4c-e, serving as a benchmark for the model's reliability and its capacity to generalize within a precise estimate range.

The multitasking capabilities of $M(P)$ are further highlighted by its performance in predicting the second parameter, voltage drop (SI). The model exhibits strong prediction accuracy with both datasets. $D_{NMC+NCA}$ shows a smaller range of predictions over increasing cycles, and D_{LCO} shows a stable range with decreasing median intervals, while the calibration accuracy and the reliability of the predictions remain high across both datasets. The performance on the third predictor, CE (SI), shows consistency and low prediction uncertainty, although the high measurement noise present in this dimension poses a challenge and makes convergence more demanding²⁶. The evaluation metrics for $M(P)$ (Supp, Table. 1) demonstrate its predictive strengths for both $D_{NMC+NCA}$ and D_{LCO} . For the D_{LCO} dataset, the voltage drop is predicted with root mean square error (RMSE) of 0.0335 and mean absolute percentage error (MAPE) of 6.6052. However, $D_{NMC+NCA}$ outperforms in CE with significantly lower error rates of 0.0256 and 0.2489 for the RMSE and MAPE, respectively. However, both datasets present higher error rates in the predicted discharge capacity. To counteract the impact of systematic noise, Median Absolute Error (medAE) is used along with MAE for a more robust error analysis. These metrics highlight $M(P)$'s versatile predictive capabilities, in handling diverse dataset requirements for multiple features and long-term predictions^{15, 33}.

We further examine $M(P)$'s performance on unseen coin cell datasets, D_{LNO} and D_{NMC} . The model predicts the voltage drop and CE well, but shows limitations and high uncertainty when predicting the discharge capacity with an RMSE of 0.5827. This may stem from the low representation of coin cells in the training data; just 4.1% of the total. To alleviate this problem, we fine-tuned the

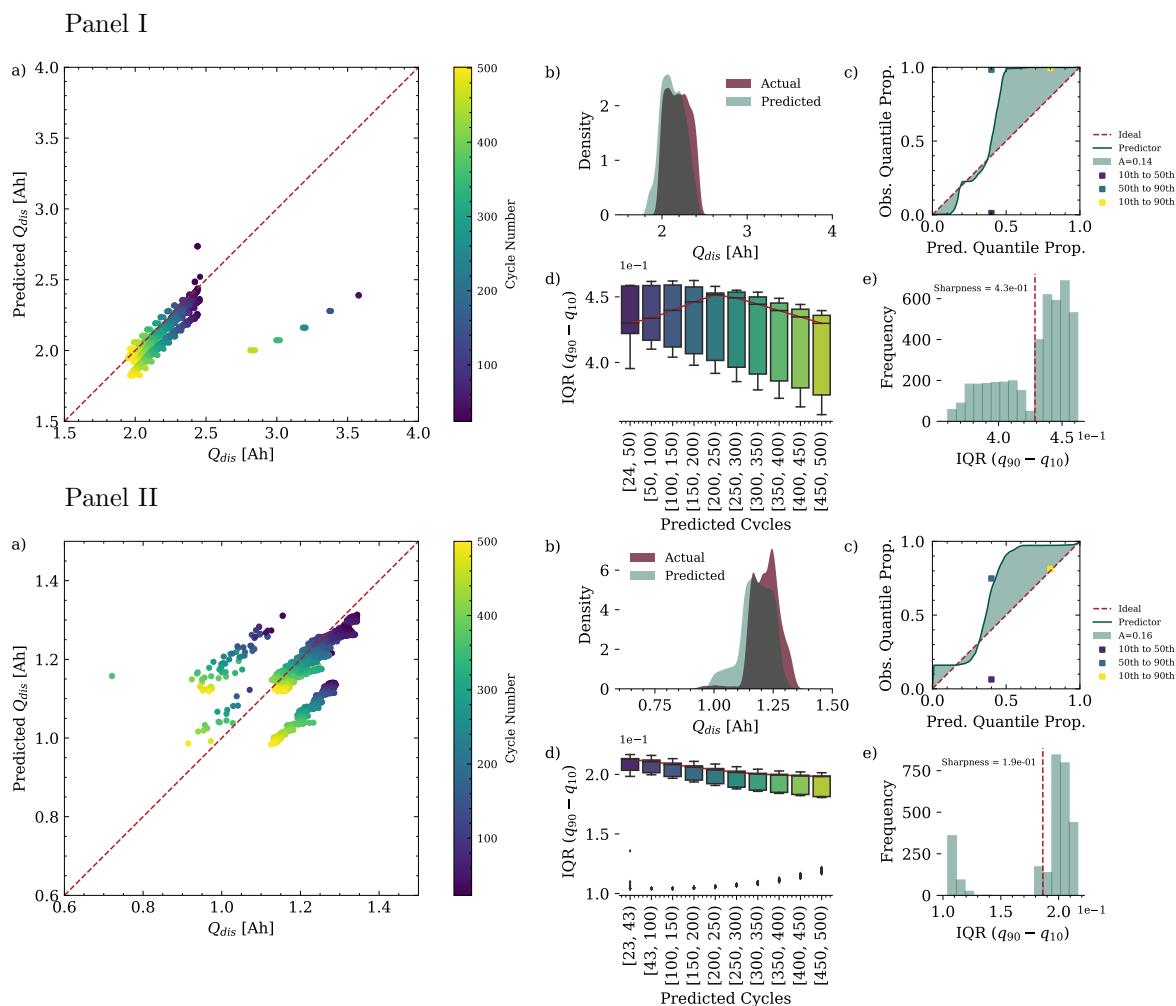


Figure 4: Comparative analysis of model predictions and its uncertainty and calibration for Q_{dis} for two datasets; $D_{NMC+NCA}$ (Panel I) and D_{LCO} (Panel II), where a) depicts the relationship between predicted and actual values of Q_{dis} , with the diagonal dashed line indicating perfect prediction accuracy, b) illustrates the density distributions of predicted versus actual Q_{dis} . The calibration plot in c) assumes a normal distribution, where the mean and standard deviation are estimated from the 10th, 50th, and 90th percentiles of predictions. It depicts the cumulative proportion of actual Q_{dis} values that fall at or below the predicted quantile values, rather than within symmetric intervals around the predictions. The ideal diagonal line represents perfect calibration with the shaded area indicating the degree of miscalibration, denoted A . The approximately diagonal trend of the calibration line up to the 0.5 quantile shows that data with residuals below the median are well described by the predictive distribution. The jump from 0.5 to 1 indicates that the predictive distribution extends further to positive values than the observed distribution of residuals; almost all test data are already covered by the predicted 0.6 quantile for both datasets. However, the overall miscalibration areas for both datasets are quite similar, indicating that despite different patterns of over- and underconfidence at specific quantiles, the general calibration performance across both datasets is comparable. Box plots at d) show the prediction intervals over multiple cycles, demonstrating the median and variability of the model prediction uncertainty over the battery's lifespan. e) provides histograms that depict the quantile-based prediction interval width between the 10th and 90th percentiles, as a measure of sharpness. The red dashed line indicates the sharpness as the mean interval width and shows the concentration of the predictive distributions that indicate narrower distribution and consequently higher confidence in predicting Q_{dis} for $D_{NMC+NCA}$ in Panel I.

313 decoder weights of $M(P)$ using the data of 17 coin cells from D_{LNO} , resulting in an updated model,
 314 $M(P)_f$. This fine-tuning process is detailed in Supp. 14, and led to a substantial improvement in
 315 predicting Q_{dis} , dropping the RMSE to 0.0002, indicating a significantly enhanced precision. $M(P)_f$'s
 316 performance will be compared with $M(B)$, trained with the BASF dataset B , in the following section.

317 2.5 Model Performance on Coin Cell Data for Generalization Insights

318 While comparing the predictive performance of models $M(B)$ and $M(P)_f$ on subsets of unseen D_{LNO}
 319 and D_{NMC} dataset (Supp. 15), $M(P)_f$ demonstrates reliable predictive alignment for voltage drop,
 320 CE, and Q_{dis} . In contrast, $M(B)$, shows a divergent pattern in voltage drop predictions, which may be
 321 due to its training on data with inherently long relaxation time profiles compared to those in D_{LNO} ,
 322 where measurements are taken shortly after state changes. However, it maintains consistency in CE
 323 predictions and adjusts Q_{dis} predictions in response to changes in the test protocol. The performance

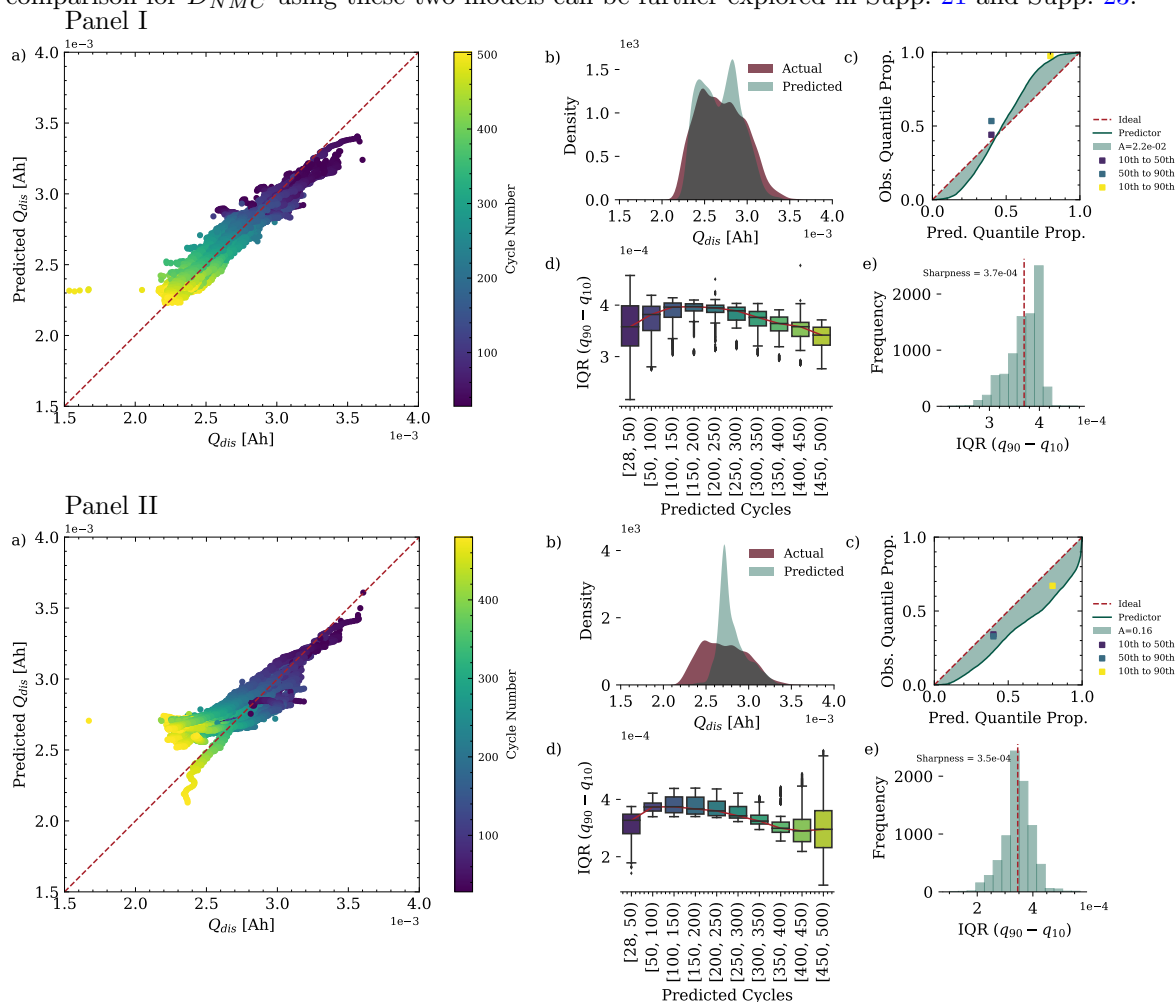


Figure 5: Performance analysis of $M(P)_f$ (Panel I) and $M(B)$ (Panel II) on D_{LNO} for Q_{dis} prediction. Plots a) illustrate the relationship between models' predictions and the actual Q_{dis} with the diagonal line representing perfect prediction accuracy, plots b) compare the density distribution of actual and predicted Q_{dis} , plots c) present calibration curves that reflect the degree of alignment between predicted probabilities and observed frequencies under a normal distribution assumption. The discrete points on the calibration curve show the observed proportions of actual values that fall within three specific intervals based on the quantiles: between the 10th and 50th, 50th and 90th, and 10th and 90th percentiles. Model $M(P)_f$ shows a high level of calibration for predicting Q_{dis} of D_{LNO} samples with a minimal miscalibrated area of 0.022. The points for 10th and 50th and 50th and 90th percentiles lie close to the diagonal line, indicating a nearly perfect calibration for these intervals. $M(B)$ exhibits a slight overconfidence by deviating from the ideal line, with a miscalibration area of 0.16. The three calibration markers for $M(B)$, are all positioned just below the diagonal line, showing uniform overconfidence across these quantile ranges, yet they remain close to this line, indicating a generally well-calibrated model. Plots d) show the prediction intervals across lifespan cycles, highlighting models' uncertainty over time and plots e) detail the distribution of prediction intervals' quantiles between the 10th and 90th percentiles, which convey the models' prediction uncertainty; a distribution skewed towards the lower quantiles suggests a higher confidence in predictions at these quantiles. The sharpness, as a measure of mean interval width, is approximately similar for both models at 3.7×10^{-4} and 3.5×10^{-4} for $M(P)_f$ and $M(B)$, respectively. Together, these plots demonstrate the $M(P)_f$'s precision in capturing discharge capacity behavior and $M(B)$'s robust generalization.

Table 2: Summary of evaluation metrics for D_{LNO}

Metrics	$M(P)_f$			$M(B)$		
	Voltage drop	CE	Q_{dis}	Voltage drop	CE	Q_{dis}
RMSE	0.0703	0.0331	0.0002	0.1247	0.0588	0.0003
MAPE	9.2285	1.1922	20.7946	34.8638	4.4560	8.8914
MAE	0.0353	0.0076	0.0001	0.0867	0.0335	0.0002
medAE	0.0181	0.0021	0.0001	0.0513	0.0104	0.0001

325 In our analysis of D_{LNO} for Q_{dis} , Fig. 5 demonstrates that $M(P)_f$ achieves high predictive fi-
326 delity. This is evident from the dense alignment of the predictions with the actual values in the scatter

327 plot (Fig. 5a), and the significant overlap in distributions seen in the density plot (Fig. 5b). The
 328 model's precision is further highlighted by concentrated prediction intervals and a calibration curve
 329 that closely traces the diagonal (Fig. 5c-e). It achieves a high proportion of data points within the pre-
 330 dictive bounds, indicative of accuracy, without excessively wide intervals that could decrease the utility
 331 of the predictions. Panel II for $M(B)$ also demonstrates a close tracking of the actual values, with
 332 a marginally broader prediction interval and higher miscalibrated area of 0.16 compared to $M(P)_f$'s
 333 of 0.022 (Panel I). Despite this variance, $M(B)$ maintains a reasonable estimate range. Qualitatively
 334 (Table 2), $M(P)_f$ achieves better accuracy in predicting Q_{dis} with a lower RMSE and MAE. $M(B)$
 335 shows higher RMSE, especially in voltage drop, and lower MAPE in Q_{dis} (8.8914) suggesting effective
 336 capture of proportional changes in the data, despite a larger absolute error. Detailed analyses of addi-
 337 tional predictive dimensions for D_{LNO} for both models and the complete dataset D_{NMC} are available
 338 in the supplementary materials. Despite the D_{LNO} data originating from another institute, the gen-
 339 eralization of $M(B)$ highlights the potential of well-trained DL models to overcome the variability of
 340 data sources.

341 2.6 Achieving chemical agnosticism

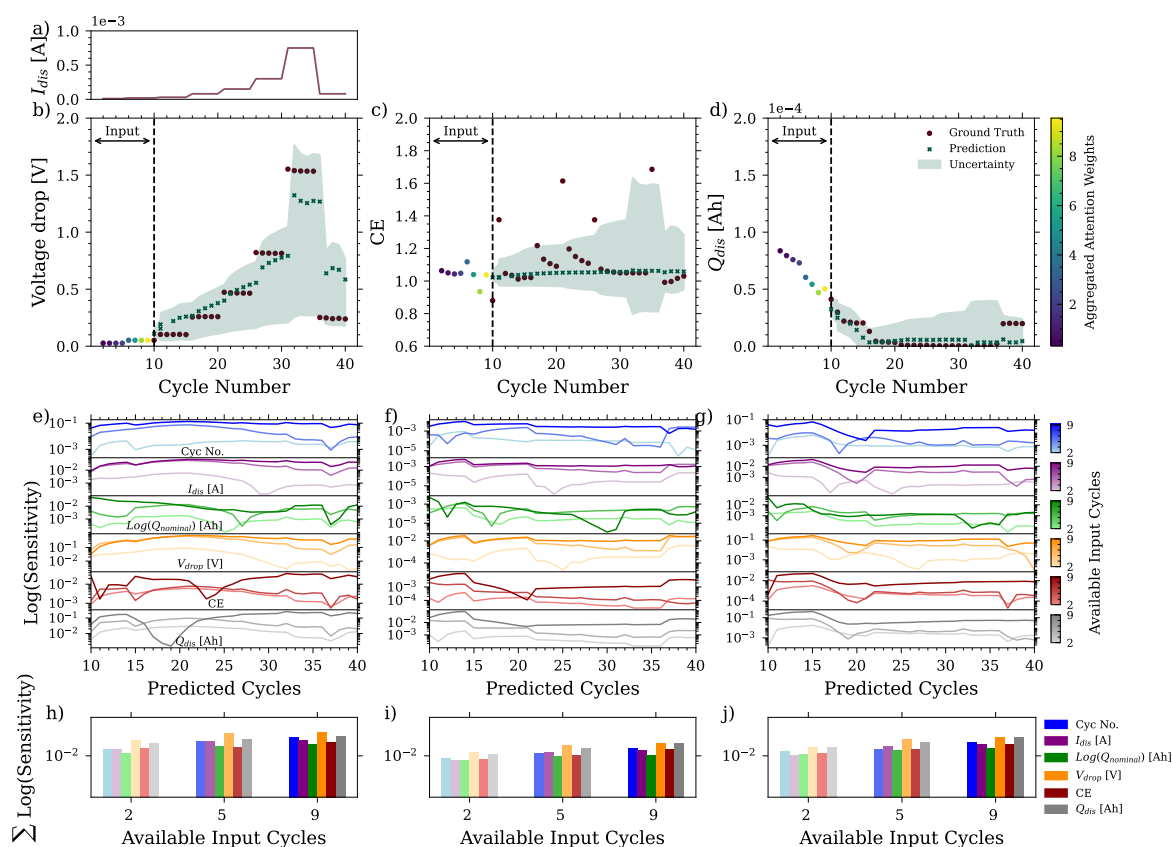


Figure 6: Analysis of $M(P)_{Na}$'s predictive accuracy and input sensitivity on Na-ion data. Plot a) presents the C-rate profile for cycling one battery, while plots b), c), and d) compare the model's prediction to actual data, showing consistency and adaptability. Sensitivity to input parameters across predicted cycles is analyzed in plots e), f), and g) on a logarithmic scale. The color intensity in these plots denotes the specific cycles from which the input parameter originates. Plots h), i), and j) show the sum of the logarithmic contribution of each input parameter towards predicting future cycles with a selective representation of three past cycle data. These visualizations confirm the model's attentive adjustment to the latest available input data and its capacity for generalization, despite the high experimental noise and limited battery performance.

342 ARCANa was so far demonstrated to generalize well across battery formats, electrolyte formu-
 343 lations, cathode chemistries and cycling procedures for LIBs. The ultimate generalization would be
 344 achieved if the model could also be deployed to Na-ion batteries. Since the underlying degradation
 345 mechanism of Na-ion batteries is very different, we performed fine-tuning to test whether $M(B)$ and
 346 $M(P)$ are capable of achieving "true chemistry agnosticism" ^{30, 16}. These fine-tuned models are deno-
 347 tated $M(B)_{Na}$ and $M(P)_{Na}$, and are trained on Na-ion cycling data with CC-CV and pulse discharge

348 settings. Details on the fine-tuning parameters are available in SI.

349 In Figures 6 and 7, we evaluate the fine-tuned $M(B)_{Na}$ and $M(P)_{Na}$ models on an unseen C-rate
 350 test protocol (Fig. 6a and Fig. 7a). Both models demonstrate flexibility in adjusting to changes in
 351 C-rates, with voltage drop, CE and Q_{dis} depicted in Fig. 6b-d and Fig. 7b-d. The model $M(B)_{Na}$
 352 shows narrower prediction intervals, indicative of lower uncertainty and greater predictive robustness.
 353 This trend is consistent across all predictive dimensions and the model is probably benefiting from the
 354 larger initial dataset on which it was trained, since it provided a richer learning environment for the
 355 model to become more 'protocol-agnostic'. Its precision is especially notable in predicting the voltage
 356 drop and CE estimations, closely following the ground-truth despite the substantial experimental noise.
 357 The aggregated attention mechanism in $M(B)_{Na}$ (Fig. 7d) also appears more fine-tuned, with greater
 358 weights on the latest cycle data, which is consistent with its precise predictions. While $M(P)_{Na}$ is
 359 adaptable, it shows a marginally wider uncertainty (Fig. 6b-d).

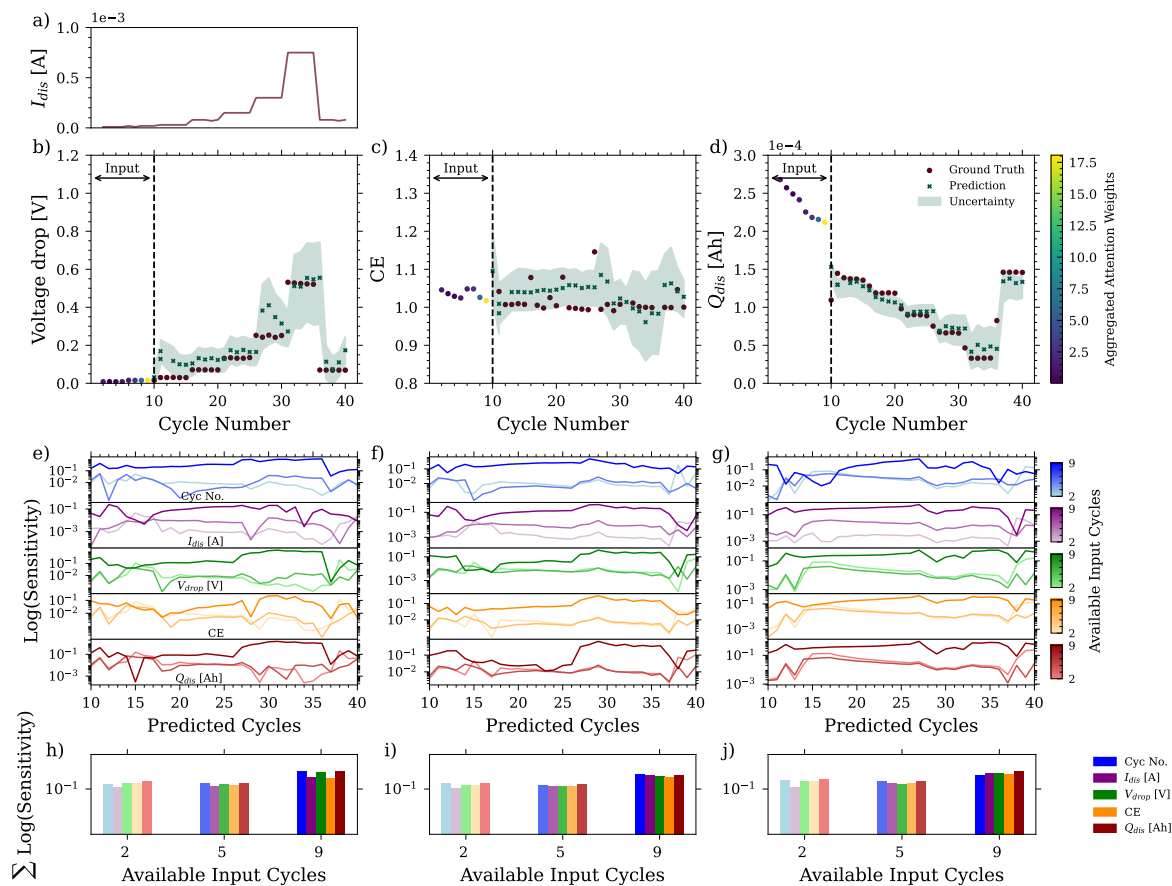


Figure 7: Evaluation of $M(B)_{Na}$'s predictive performance and input sensitivity on our own Na-ion data. Plot a) shows the discharge current profile, while plots b), c), and d) depict the predictions for voltage drop, CE and Q_{dis} against the ground truth. The colorbar here shows the aggregated attention weights across the input data. Plots e-g) provide a detailed logarithmic sensitivity analysis per predictive cycle for each input parameter, and plots h-j) aggregate these sensitivities, highlighting the model's focus on different input cycles, especially the most recent ones, reflecting $M(B)_{Na}$'s protocol adaptability and robust response to experimental noise.

360 Sensitivity analysis, as shown in Figures 7e-g and 6e-g evaluates the input parameter influence
 361 on future predictions for $M(B)_{Na}$ and $M(P)_{Na}$. Both models demonstrate increased sensitivity to
 362 the most recent input data, i.e. cycles 7 to 9 in this provided example, aligned with their attention
 363 distributions, with cycle 9 receiving the highest attention. This increased emphasis on the last input
 364 cycles corresponds to the rapid degradation patterns in this sodium coin cell. As the model receives
 365 each successive cycle, the most recent data, here cycle 9, becomes important in shaping its predictions,
 366 allowing the model to more accurately predict ongoing trends.

367 In Fig. 7, $M(B)_{Na}$ shows a greater overall sensitivity across input cycles, particularly for the di-
 368 mensions of voltage drop and Q_{dis} . This is further illustrated in sensitivity profiles and cumulative
 369 plots (Fig. 7h-j) highlighting a refined input-response relationship and a lower uncertainty interval in

370 the primary prediction (Fig. 7a-c). Such a distinct sensitivity indicates $M(B)_{Na}$'s ability to precisely
 371 identify and respond to subtle variations. Despite the high experimental noise and limited battery per-
 372 formance, the saliency and attention trends of both models remain remarkably similar. This suggests
 373 that both mechanisms are intrinsic to the model's architecture, enabling them to perform consistently
 374 at diverse scenarios.

375 To further substantiate our initial findings, the plots in Fig. 8, show both models' Q_{dis} predictions
 376 aligning well with the ground-truth. $M(P)_{Na}$ exhibit a tighter clustering around the actual values,
 377 while $M(B)_{Na}$ exhibits a broader spread. The prediction intervals and the distribution of quantiles
 378 across the 10th and 90th percentile for both models confirm their consistency and calibrated confi-
 379 dence. These evaluations provide insights into the model's robustness. The performance of $M(B)_{Na}$'s
 380 especially underscores the advantage of extensive and diverse pretraining datasets in enhancing model
 381 generalization across different battery chemistries.

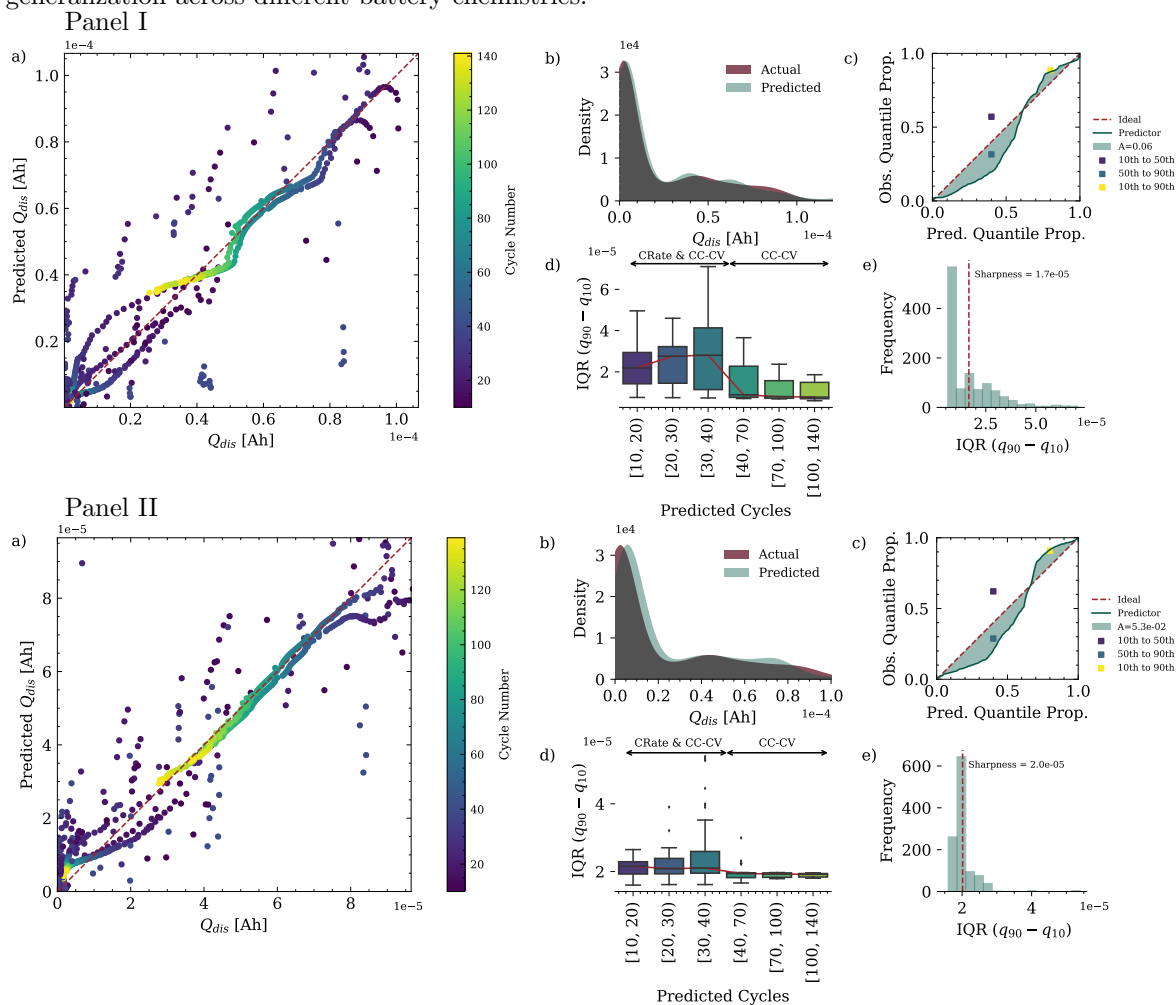


Figure 8: comparative Q_{dis} prediction analysis for Na-ion batteries using $M(P)_{Na}$ (Panel I) and $M(B)_{Na}$ (Panel II). The scatter plots a) illustrate the models' alignment with actual measurements. Density plots b) compare the distributions of predicted and actual values, demonstrating the models' accuracy in estimating Q_{dis} . Calibration plots in c) depict how well the predicted probabilities match the observed outcomes against the benchmark line, with the discrete points representing the observed proportions of actual values that fall within three quantile intervals. Both models demonstrate a pattern of marginal overconfidence below the 70th percentile and a slight underconfidence above this percentile, as evidenced by the calibration points's positions beneath and above the diagonal line, respectively. $M(P)_{Na}$ shows a larger area of divergence, $A = 0.06$, while $M(B)_{Na}$ presents a closer fit with a miscalibration of 0.053, highlighting both models' well-calibrated prediction capabilities across different chemistries. Boxplots d) visualize the spread and consistency of prediction intervals across predicted cycles. Histograms in e) represent the distribution of the quantile intervals of the models' prediction, highlighting uncertainty; these distributions indicate where, within the prediction range, the models' confidence is concentrated, with sharpness values of 1.7×10^{-5} for $M(P)_{Na}$ and 2.0×10^{-5} for $M(B)_{Na}$, demonstrating a precise estimation of uncertainty.

3 Discussion

We demonstrated the chemistry-, format- and cycling procedure-agnostic ARCANA framework, and its ability to reliably monitor battery life and SOH by utilizing multitask learning with an attention mechanism. ARCANA excelled across three predictive settings, demonstrating that augmenting the model with diverse knowledge streams enhances its generalization across virtually all variations possible in batteries such as anode, cathode, electrolyte and shuttle ion chemistry and format. The ARCANA model integrates uncertainty quantification and attention mechanisms for each and every cycle to elucidate the model’s focus for each prediction and is essential for uncovering complex patterns associated across multiple factors. Further evaluation involves saliency and sensitivity assessments, allowing us to understand the impact of perturbation of input parameter on output predictions. By examining whether saliency and attention are directly correlated or orthogonal to each other, we gain a comprehensive understanding of input-output relationships, increasing the model’s explainability and reliability in extrapolation. Incorporating raw data and failed experiments, as suggested in prior studies^{45, 15} is a deliberate strategy to teach our models to recognize variations across similar cell types and manufactures. This inclusion not only enables uncertainties to be quantified more accurately but also deepens reliability insights, reduces bias, and offers a more meaningful understanding of the data. A conceptually straightforward extension to this work would be to incorporate additional features, such as the rate of change of voltage with respect to capacity (dQ/dV)^{35, 12}, and leverage different characterization methods like spectroscopy, to enhance the predictive power of the models. This will not only enhance multi-feature predictions, but also deepen the understanding of degradation processes^{15, 33, 51}.

We observed that $M(P)$, trained on public data, offers broader generalization across various battery types and protocols, albeit with increased uncertainty. $M(B)$, trained on a more extensive dataset, demonstrates a lower uncertainty. This further motivates the importance of data sharing and management. Our findings also reveal that fine-tuning the models with few labels significantly improves their generalization to new chemistries, especially for $M(B)$. The methodology outlined in this paper presents an opportunity for other researchers to create their own high-performance models. By retraining or fine-tuning with different datasets, researchers can tailor these predictive models to their specific experimental setups and desired outcomes. This flexibility allows for the exploration of different perspectives and approaches, facilitating the development of more accurate and specialized models. One could envision a model-sharing and transfer-learning community similar to those found today in the fields of computer vision and language modeling. Furthermore, the performance metrics explored here raise the tantalizing prospect of further improving model quality via a federated learning approach. This could enable researchers from diverse backgrounds and institutions to pool their data and expertise, leading to more powerful models.

The modular design of the ARCANA pipeline enables real-time monitoring of battery degradation profiles, promoting timely and cost-effective interventions. This proactive approach prevents prolonged suboptimal testing conditions, improving the R&D process, and contributes to more informed material selection and protocol optimization. By automating data collection, processing, and analysis, researchers can streamline their experimental workflows and reduce human error. Furthermore, ML models can continuously learn from new data, adapt to evolving experimental conditions, and provide real-time insights. This integration of ML and laboratory workflows has the potential to transform battery research, enabling researchers to make data-driven decisions, uncover novel insights more rapidly and accelerating the pace of discovery.

Overall, we demonstrated that incorporating multitask learning with an attention mechanism creates a framework that can achieve chemistry agnosticism as envisioned by Battery 2030+⁵ and the interesting fact that a DL architecture trained on a smaller, noisier, but more diverse dataset yields better generalization at the cost of higher uncertainty. We hope that the pipeline will emerge as an indispensable and transformative tool to bridge the gap between lab-scale research and commercial viability, and will become essential for development of applications and insightful predictive models in the energy storage field.

4 Methods

4.1 Model compartments Dynamics

In the following section, some of the key components of the ARCANA framework are explained to underscore their contribution to the overall efficacy and reliability of the model. This includes an exploration of attention mechanisms, a teacher forcing scheduler, methods to quantify predictive uncertainty, a strategic early stopping protocol, a training procedure, and evaluation metrics.

Attention mechanism

Within the proposed ARCANA framework, two distinct attention mechanisms are implemented. The first, termed additive attention, is also known as Bahdanau attention⁸. This mechanism aligns the hidden state of the decoder h_t at each time step t with the hidden states of the encoder (h_s), thus producing a context vector that encapsulates the weighted relevance of each historical temporal segment from the past cycles. This vector provides a dynamically focused representation of the input sequence pertinent to the current decoding step. This mechanism is functional through a parameterized attention model. The model calculates an attention score e_{ts} (Eq. 1) for each encoder state h_s given by:

$$e_{ts} = v^T \tanh(W_1 h_t + w_2 h_s) \quad (1)$$

where W_1 and W_2 are the weight matrices that transform the respective hidden states into a common feature space and v is a weight vector that projects the activated sum into a scalar score. Attention weights α_{ts} are then determined by normalizing these scores using the softmax function (Eq. 2).

$$\alpha_{ts} = \frac{\exp(e_{ts})}{\sum_{k=1}^{T_e} \exp(e_{tk})} \quad (2)$$

here, T_e is the total number of time steps in the encoder sequence.

The context vector c_t results from aggregating the encoder hidden states, each weighted by its respective attention weight, as can be seen in Eq. 3, and can improve the model's capacity for handling Seq-to-Seq predictions⁴¹.

$$c_t = \sum_{s=1}^{T_e} \alpha_{ts} h_s \quad (3)$$

Another attention mechanism that can be employed within the ARCANA architecture is multihead attention. This mechanism expands the model's capacity to focus on different positions of the input sequence simultaneously⁴⁹, which is crucial for capturing a wider range of dependencies inherent in battery lifetime data. This attention mechanism operates by projecting the decoder's hidden states and the encoder outputs, representing the past cycle's information, into multiple subspaces. This is formulated as: (Eq. 4)

$$\text{MultiHead}(Q, K, V) = \text{Concat}(\text{head}_1, \dots, \text{head}_h) W^0 \quad (4)$$

$$\text{head}_i = \text{Attention}(QW_i^Q, KW_i^K, VW_i^V) \quad (5)$$

where each head (head_i) captures different aspects of the input data and is computed as shown in Eq.5. The operation applied in each head is defined by the attention of the scaled dot product and is presented in Eq. 6.

$$\text{Attention}(Q, K, V) = \text{softmax}\left(\frac{QK^T}{\sqrt{d_k}}\right) V \quad (6)$$

Here, Q , K , and V are the query, key, and value matrices, respectively. Q is generated from the hidden states of the decoder, while K and V are derived from the encoder outputs. This arrangement enables the decoder to integrate the current state information with historical data provided by the encoder. The parameter matrices W_i^Q , W_i^K , and W_i^V for each head i , along with the output weight matrix W^0 , are optimized during the training process. These matrices are instrumental in transforming the input data into different representational subspaces to capture various aspects and dependencies within the data. The parameter d_k , representing the dimension of the key vectors, scales the dot product within the attention mechanism. In Eq. 6, the softmax function is applied to these scaled attention scores, which originate from the interactions between the query and key matrices. This process results in the production of a context vector, which integrates information from different representational subspaces and allows the model to consider multiple aspects of historical data^{65, 60}.

Teacher forcing

Teacher forcing optimizes the learning of temporal dependencies. By integrating the real data from previous time steps, the technique promotes rapid stabilization and convergence of the model. In the present study, the implementation of the teacher forcing strategy is applied through a calculated division of training epochs. This division is reflective of the model's incremental improvement in processing sequences with varying lengths over time by prioritizing shorter sequences at the early stages of training to ensure intensive guidance. This preferential focus ensures that the model does not prematurely plateau when learning to predict longer-term dependencies.

To quantitatively define this approach, the training period consisting of E epochs is divided into D equal segments s . Within the i -th segment, the teacher forcing ratio is adjusted through a decay parameter λ , which represents how quickly the training procedure switches from using real data as decoder inputs to using model predictions from the previous cycle, as depicted in Fig.2b. The allocation of epochs per division d_i is calculated as can be seen in Eq. 7

$$d_i = \text{round}\left(\frac{s \cdot e^{-\lambda i}}{\sum_{j=0}^{D-1} s \cdot e^{-\lambda j}} \cdot E\right) \quad (7)$$

Following this, the teacher forcing ratio for the t -th epoch in the i -th segment is linearly reduced from a starting ratio R_{start} to an ending ratio R_{end} , using the following equation, Eq. 8.

$$A = \left(\frac{R_{start} - R_{end}}{d_i + \epsilon}\right) \quad (8)$$
$$R_{t_i} = R_{start} - A \cdot t$$

Here, R_{t_i} indicates the teacher forcing ratio at epoch t for the i -th segment. The expression A represents the decrease per epoch in that segment. To ensure numerical stability and avoid division by zero, a small constant ϵ , set to 10^{-8} , is included in the calculation as indicated in Eq. 8. The teacher forcing ratio, as a probabilistic measure, represents the likelihood that the model will utilize the actual observation from the training data at a given prediction step. This approach modulates the ratio to facilitate a smooth transition from guided to self-generated sequence prediction. The adjusted ratios are indicative of the model's learning trajectory, enhancing its independent predictive accuracy across different sequence lengths.

Uncertainty quantification

The pinball loss, in this study, provides a robust metric for predicting a range of potential outcomes, rather than a single point estimation. This is an effective measure for forecasting scenarios where the impacts of overprediction and underprediction are asymmetric⁵⁷. It is defined for a set of quantiles $Q = \{q_1, q_2, q_3\}$ where $q_1 < q_2 < q_3$ and in this study, we select $Q = \{0.1, 0.5, 0.9\}$ corresponding to the 10-th, 50-th, and 90-th percentiles, respectively. For a given predicted value \hat{y} and the actual target value y , the pinball loss for a single quantile q is calculated as:

$$L_q(\hat{y}, y) = \begin{cases} (1 - q) \cdot (\hat{y} - y) & \text{if } y < \hat{y} \\ q \cdot (y - \hat{y}) & \text{if } y \geq \hat{y} \end{cases} \quad (9)$$

In the implementation of this loss function, a mask is provided and applied to each quantile's loss to selectively evaluate certain predictions, allowing for the exclusion of outliers. The total pinball loss for multiple quantiles is then the sum of the individual losses for each quantile, averaged over all predictions, as shown in Eq. 10, reflecting the model's performance across the specified range of quantiles.

$$L(Q, \hat{Y}, Y) = \frac{1}{N} \sum_{i=1}^N \sum_{q \in Q} L_q(\hat{y}_{qi}, y_i) \quad (10)$$

Here, N is the number of observations, \hat{Y} is a stack of vectors, with each vector containing the predictions for all observations at one of the specified quantiles, and Y is the vector of the true target values. Each element \hat{y}_{qi} in \hat{Y} denotes the predicted value for the i -th observation at quantile q . This configuration not only facilitates efficient computation of the loss function across multiple quantiles and observations, but also captures the central tendency and variability of the predictions, making it a comprehensive loss function for probabilistic forecasting^{57, 37}.

511 Early stopping

512 To optimize training, a rigorous early stopping approach is incorporated. This method was originally
513 proposed by Prechelt et al. ⁴⁴ and combines criteria to prevent overfitting while ensuring substantial training
514 progress, especially in the presence of noisy data. Here, a dual-criteria strategy is implemented. The first
515 criterion assesses the ratio between generalization loss (GL) and training progress, which is shown in Eq.11,
516 where E_{val} represents the validation error at the current epoch, $E_{min\ val}$ is the lowest validation error obtained
517 up to the current epoch, and $E_{train\ strip}$ denotes the training errors within a recent sequence of epochs. This
518 sequence, or strip, is a designated period in which progress quotient (PQ) is measured. If the generalization-
519 loss-to-progress-quotient-ratio (GL/PQ) surpasses a predefined value, it may indicate that further training will
520 not be beneficial for the model’s generalizability.

$$GL = 100 \cdot \left(\frac{E_{val}}{E_{min\ val}} - 1 \right)$$
$$PQ = 1000 \cdot \left(\frac{Mean(E_{train\ strip})}{Min(E_{train\ strip})} - 1 \right)$$
(11)

521 The second criterion implements a conventional check and is applied to monitor the trend in validation
522 error. An increased trend over the epoch sequence suggests that overfitting could be occurring. Training
523 is discontinued when both the ratio criterion and the error-trend criterion indicate that further training is
524 unlikely to yield significant gains. In general, this strategy offers a control mechanism that aligns the duration
525 of training with the achievement of a well-generalized model capable of accurate predictions.

526 Training Procedure

527 Expanding on Seq-to-Seq integration, the training phase begins by initializing the data loaders for batch
528 processing and configuring the parameters of the Seq-to-Seq model, the loss criteria, the optimizer, and a
529 dynamic learning rate scheduler ²⁶. Hyperparameter optimization, through a series of trials using Optuna’s ⁴
530 Tree-structured Parzen Estimator (TPE) Sampler, employs a probabilistic model to specify the most promising
531 parameter configuration, navigating the search space while balancing exploration and exploitation within a
532 complex and high-dimensional domain ¹⁰. Training unfolds over several epochs, with each iteration starting
533 with a reset of the model’s hidden states and zeroing gradients to ensure clean computation for the forward
534 pass. The pinball loss function is selected for its effectiveness in probabilistic forecasting, eliminating the need
535 for a presumptive data distribution model ³⁷ unlike traditional metrics ⁵⁷, which are more sensitive to noise and
536 anomalies. These asymmetric and non-parametric criteria assess forecast accuracy by penalizing deviations
537 from three targeted quantiles, namely 0.1, 0.5, and 0.9, enhancing robustness to outliers and the efficacy for
538 LSTM-based networks ⁵⁷. At the same time, a masking technique ³³ is implemented to filter out padding-
539 induced distortions from the loss calculation, ensuring the integrity of the learning signal. Backpropagation
540 follows loss computation, incorporating gradient clipping to prevent divergence and gradient explosion in
541 recurrent network architectures. Additionally, learning rate adjustments encourage robust convergence. The
542 validation phase alternates with training, where performance is assessed and early stopping criteria are applied
543 to mitigate overfitting. Optuna enhances optimization by pruning the less promising trials. Once the training
544 is completed, the model parameters are saved and a comprehensive report is generated detailing the training
545 results. The training procedure steps described are schematically depicted in Supp.1

546 Evaluation metrics

547 For this study, the following metrics are implemented, including both average errors and variability of indi-
548 vidual predictions, to evaluate the performance of the model. These metrics are RMSE (Eq. 12) which provides
549 a measure of the magnitude of prediction errors, MAPE (Eq. 13) which measures the average magnitude of
550 errors as a percentage, medAE (Eq. 14) to capture the median error, reducing the influence of outliers, and
551 mean absolute error (MAE) (Eq. 15) which represents the mean absolute differences.

$$RMSE = \sqrt{\frac{1}{n} \sum_{i=1}^n (y_i - \hat{y}_i)^2}$$
(12)

$$MAPE = \frac{100\%}{n} \sum_{i=1}^n \left| \frac{y_i - \hat{y}_i}{y_i} \right|$$
(13)

$$medAE = \text{median}(|y_i - \hat{y}_i| : i = 1, 2, \dots, n)$$
(14)

$$MAE = \frac{1}{n} \sum_{i=1}^n |y_i - \hat{y}_i|$$
(15)

Data and code availability

Open source data supporting the findings of this study are available online, with access details provided in Table. 1. The ARCANA framework can be installed using `pip install arcana-batt` or cloned from <https://github.com/basf/ARCANA>. In addition, public pre-trained model weights can be accessed at <https://doi.org/10.5281/zenodo.10293072>.

Acknowledgements

This work contributes to TUM.Battery, the Munich Data Science Institute, and the Munich Institute for Robotic and Machine Intelligence. This work contributes to the research performed at CELEST (Center for Electrochemical Energy Storage Ulm-Karlsruhe) and was partly funded by the German Research Foundation (DFG) under Project ID 390874152 (POLiS Cluster of Excellence). This project also received funding from the European Union’s Horizon 2020 research and innovation program under grant agreement No 957189. The project is part of BATTERY 2030+, the large-scale European research initiative for inventing sustainable batteries for the future, funded by European Union’s Horizon 2020 research and innovation program under Grant Agreement No. 957213. HSS acknowledges funding from German Research Foundation (DFG) under Project ID 390776260 (eConversion Cluster of Excellence).

Author contributions statement

K.M. and B.B. provided the comprehensive BASF dataset, L.M. and L.N. conducted all cycling data for Li-ion and Na-ion batteries at KIT/ IPC respectively. Data assembly, data cleaning, model idea including the design architecture, implementation, training, evaluation, and package creation is conducted by F.R.. R.L., D.L. supervised the model development. K.M., B.B., H.S., R.L, and D.L. supervised this research. All authors reviewed the manuscript.

Conflicts of interest

The authors have no competing or financial interests to declare.

References

- [1] Toyota Research Institute. Experimental data platform. 2021. *Project Closed-loop optimization of extreme fast charging for batteries using machine learning*. URL: <https://data.matr.io/1/projects/5d80e633f405260001c0b60a>.
- [2] Toyota Research Institute. Experimental data platform. 2021. *Project Data-driven prediction of battery cycle life before capacity degradation*. URL: <https://data.matr.io/1/projects/5c48dd2bc625d700019f3204>.
- [3] Haruna Adamu et al. “Artificial intelligence-navigated development of high-performance electrochemical energy storage systems through feature engineering of multiple descriptor families of materials”. In: *Energy Advances* 2.5 (2023), pp. 615–645. DOI: [10.1039/D3YA00104K](https://doi.org/10.1039/D3YA00104K).

- 588 [4] Takuya Akiba et al. “Optuna: A next-generation hyperparameter optimization framework”.
589 In: *Proceedings of the 25th ACM SIGKDD international conference on knowledge discovery &*
590 *data mining*. Ed. by Association for Computing Machinery. Royal Society of Chemistry, 2019,
591 pp. 2623–2631. DOI: [10.1145/3292500.3330701](https://doi.org/10.1145/3292500.3330701).
- 592 [5] Julia Amici et al. “A roadmap for transforming research to invent the batteries of the future
593 designed within the European large scale research initiative BATTERY 2030+”. In: *Advanced*
594 *energy materials* 12.17 (2022), p. 2102785. DOI: [10.1002/aenm.202102785](https://doi.org/10.1002/aenm.202102785).
- 595 [6] Peter M Attia et al. ““Knees” in lithium-ion battery aging trajectories”. In: *Journal of The*
596 *Electrochemical Society* 169.6 (2022), p. 060517. DOI: [10.1149/1945-7111/ac6d13](https://doi.org/10.1149/1945-7111/ac6d13).
- 597 [7] Peter M Attia et al. “Closed-loop optimization of fast-charging protocols for batteries with
598 machine learning”. In: *Nature* 578.7795 (2020), pp. 397–402. DOI: [10.1038/s41586-020-1994-](https://doi.org/10.1038/s41586-020-1994-5)
599 [5](https://doi.org/10.1038/s41586-020-1994-5).
- 600 [8] Dzmitry Bahdanau, Kyunghyun Cho, and Yoshua Bengio. “Neural Machine Translation by
601 Jointly Learning to Align and Translate”. In: (2016). DOI: [10.48550/arXiv.1409.0473](https://doi.org/10.48550/arXiv.1409.0473). arXiv:
602 [1409.0473](https://arxiv.org/abs/1409.0473).
- 603 [9] Thorsten Baumhöfer et al. “Production caused variation in capacity aging trend and correlation
604 to initial cell performance”. In: *Journal of Power Sources* 247 (2014), pp. 332–338. DOI: [10.](https://doi.org/10.1016/j.jpowsour.2013.08.108)
605 [1016/j.jpowsour.2013.08.108](https://doi.org/10.1016/j.jpowsour.2013.08.108).
- 606 [10] James Bergstra et al. “Algorithms for Hyper-Parameter Optimization”. In: *Advances in Neu-*
607 *ral Information Processing Systems*. Ed. by J. Shawe-Taylor et al. Vol. 24. Curran Associates,
608 Inc., 2011. URL: [https://proceedings.neurips.cc/paper_files/paper/2011/file/](https://proceedings.neurips.cc/paper_files/paper/2011/file/86e8f7ab32cfd12577bc2619bc635690-Paper.pdf)
609 [86e8f7ab32cfd12577bc2619bc635690-Paper.pdf](https://proceedings.neurips.cc/paper_files/paper/2011/file/86e8f7ab32cfd12577bc2619bc635690-Paper.pdf).
- 610 [11] Arghya Bhowmik et al. “Implications of the BATTERY 2030+ AI-Assisted Toolkit on Future
611 Low-TRL Battery Discoveries and Chemistries”. In: *Advanced Energy Materials* 12.17 (2022),
612 p. 2102698. DOI: [10.1002/aenm.202102698](https://doi.org/10.1002/aenm.202102698).
- 613 [12] Ira Bloom et al. “Differential voltage analyses of high-power, lithium-ion cells: 1. Technique
614 and application”. In: *Journal of Power Sources* 139.1-2 (2005), pp. 295–303. DOI: [10.1016/j.](https://doi.org/10.1016/j.jpowsour.2004.07.021)
615 [jpowsour.2004.07.021](https://doi.org/10.1016/j.jpowsour.2004.07.021).
- 616 [13] JC Burns et al. “Evaluation of effects of additives in wound Li-ion cells through high precision
617 coulometry”. In: *Journal of The Electrochemical Society* 158.3 (2011), A255. DOI: [10.1149/1.](https://doi.org/10.1149/1.3531997)
618 [3531997](https://doi.org/10.1149/1.3531997).
- 619 [14] JC Burns et al. “Predicting and extending the lifetime of Li-ion batteries”. In: *Journal of The*
620 *Electrochemical Society* 160.9 (2013), A1451. DOI: [10.1149/2.060309jes](https://doi.org/10.1149/2.060309jes).
- 621 [15] Yunhong Che et al. “Health prognostics for lithium-ion batteries: mechanisms, methods, and
622 prospects”. In: *Energy & Environmental Science* 16.2 (2023), pp. 338–371. DOI: [10.1039/](https://doi.org/10.1039/D2EE03019E)
623 [D2EE03019E](https://doi.org/10.1039/D2EE03019E).
- 624 [16] Guzhong Chen et al. “Generalizing property prediction of ionic liquids from limited labeled data:
625 a one-stop framework empowered by transfer learning”. In: *Digital Discovery* 2.3 (2023), pp. 591–
626 601. DOI: [10.1039/D3DD00040K](https://doi.org/10.1039/D3DD00040K).
- 627 [17] Tim Cooijmans et al. “Recurrent Batch Normalization”. In: (2017). arXiv: [1603.09025](https://arxiv.org/abs/1603.09025) [[cs.LG](https://arxiv.org/abs/1603.09025)].
- 628 [18] JR Dahn, JC Burns, and DA Stevens. “Importance of coulombic efficiency measurements in
629 R&D efforts to obtain long-lived Li-ion batteries”. In: *The Electrochemical Society Interface* 25.3
630 (2016), p. 75. DOI: [10.1149/2.F07163if](https://doi.org/10.1149/2.F07163if).
- 631 [19] Valerio De Angelis, Yuliya Preger, and Babu R Chalamala. *Battery Lifecycle Framework: A*
632 *Flexible Repository and Visualization Tool for Battery Data from Materials Development to Field*
633 *Implementation*. Mar. 2021. DOI: [10.1149/osf.io/h7c24](https://doi.org/10.1149/osf.io/h7c24). URL: [osf.io/preprints/ecsarxiv/](https://osf.io/preprints/ecsarxiv/h7c24)
634 [h7c24](https://osf.io/preprints/ecsarxiv/h7c24).
- 635 [20] Zhongwei Deng et al. “Battery health estimation with degradation pattern recognition and trans-
636 fer learning”. In: *Journal of Power Sources* 525 (2022), p. 231027. DOI: [10.1016/j.jpowsour.](https://doi.org/10.1016/j.jpowsour.2022.231027)
637 [2022.231027](https://doi.org/10.1016/j.jpowsour.2022.231027).

- 638 [21] Sandia National Laboratories Grid Energy Storage Department. *Battery Archive. Homepage of*
639 *Battery Archive*. [Online; accessed 31-July-2023]. 2021. URL: <https://www.batteryarchive.org>.
640
- 641 [22] Gonalo Dos Reis et al. “Lithium-ion battery data and where to find it”. In: *Energy and AI* 5
642 (2021), p. 100081. DOI: [10.1016/j.egyai.2021.100081](https://doi.org/10.1016/j.egyai.2021.100081).
- 643 [23] Claudia Draxl and Matthias Scheffler. “NOMAD: The FAIR concept for big data-driven materials
644 science”. In: *Mrs Bulletin* 43.9 (2018), pp. 676–682. DOI: [10.1557/mrs.2018.208](https://doi.org/10.1557/mrs.2018.208).
- 645 [24] Maximilian Fichtner et al. “Rechargeable batteries of the future - the state of the art from a
646 BATTERY 2030+ perspective”. In: *Advanced Energy Materials* 12.17 (2022), p. 2102904.
- 647 [25] Tilmann Gneiting, Fadoua Balabdaoui, and Adrian E Raftery. “Probabilistic forecasts, calibra-
648 tion and sharpness”. In: *Journal of the Royal Statistical Society Series B: Statistical Methodology*
649 69.2 (2007), pp. 243–268. DOI: [10.1111/j.1467-9868.2007.00587.x](https://doi.org/10.1111/j.1467-9868.2007.00587.x).
- 650 [26] Yoav Goldberg. “A primer on neural network models for natural language processing”. In: *Journal*
651 *of Artificial Intelligence Research* 57 (2016), pp. 345–420. DOI: [10.1613/jair.4992](https://doi.org/10.1613/jair.4992).
- 652 [27] Qingrui Gong, Ping Wang, and Ze Cheng. “An encoder-decoder model based on deep learning
653 for state of health estimation of lithium-ion battery”. In: *Journal of Energy Storage* 46 (2022),
654 p. 103804. DOI: [10.1016/j.est.2021.103804](https://doi.org/10.1016/j.est.2021.103804).
- 655 [28] Chuan Guo et al. “On Calibration of Modern Neural Networks”. In: *Proceedings of the 34th*
656 *International Conference on Machine Learning*. Ed. by Doina Precup and Yee Whye Teh. Vol. 70.
657 Proceedings of Machine Learning Research. PMLR, Aug. 2017, pp. 1321–1330. URL: <https://proceedings.mlr.press/v70/guo17a.html>.
658
- 659 [29] CALCE battery research group homepage. URL: <https://calce.umd.edu/data>.
- 660 [30] Swarn Jha et al. “Learning-assisted Materials Development and Device Management in Bat-
661 teries and Supercapacitors: Performance Comparison and Challenges”. In: *Journal of Materials*
662 *Chemistry A* 11.8 (2023), pp. 3904–3936. DOI: [10.1039/D2TA07148G](https://doi.org/10.1039/D2TA07148G).
- 663 [31] MM Kabir and Dervis Emre Demirocak. “Degradation mechanisms in Li-ion batteries: a state-
664 of-the-art review”. In: *International Journal of Energy Research* 41.14 (2017), pp. 1963–1986.
665 DOI: [10.1002/er.3762](https://doi.org/10.1002/er.3762).
- 666 [32] Weihan Li et al. “Digital twin for battery systems: Cloud battery management system with
667 online state-of-charge and state-of-health estimation”. In: *Journal of energy storage* 30 (2020),
668 p. 101557. DOI: [10.1016/j.est.2020.101557](https://doi.org/10.1016/j.est.2020.101557).
- 669 [33] Weihan Li et al. “Forecasting battery capacity and power degradation with multi-task learning”.
670 In: *Energy Storage Materials* 53 (2022), pp. 453–466. DOI: [10.1016/j.ensm.2022.09.013](https://doi.org/10.1016/j.ensm.2022.09.013).
- 671 [34] Weihan Li et al. “One-shot battery degradation trajectory prediction with deep learning”. In:
672 *Journal of Power Sources* 506 (2021), p. 230024. DOI: [10.1016/j.jpowsour.2021.230024](https://doi.org/10.1016/j.jpowsour.2021.230024).
- 673 [35] Xiaoyu Li, Zhenpo Wang, and Jinying Yan. “Prognostic health condition for lithium battery
674 using the partial incremental capacity and Gaussian process regression”. In: *Journal of power*
675 *sources* 421 (2019), pp. 56–67. DOI: [10.1016/j.jpowsour.2019.03.008](https://doi.org/10.1016/j.jpowsour.2019.03.008).
- 676 [36] Chen Ling. “A review of the recent progress in battery informatics”. In: *npj Computational*
677 *Materials* 8.1 (2022), p. 33. DOI: [10.1038/s41524-022-00713-x](https://doi.org/10.1038/s41524-022-00713-x).
- 678 [37] Bidong Liu et al. “Probabilistic load forecasting via quantile regression averaging on sister fore-
679 casts”. In: *IEEE Transactions on Smart Grid* 8.2 (2015), pp. 730–737. DOI: [10.1109/TSG.2015.2437877](https://doi.org/10.1109/TSG.2015.2437877).
680
- 681 [38] Leon Merker. *2023 Commercial Coincell 45mAh*. Version 1.0. Nov. 2023. DOI: [10.5281/zenodo.](https://doi.org/10.5281/zenodo.10102627)
682 [10102627](https://doi.org/10.5281/zenodo.10102627). URL: <https://doi.org/10.5281/zenodo.10102627>.
- 683 [39] Leon Merker. *InZePro InForm 300 Cycles CCCV after EOL*. Version 1.0. Nov. 2023. DOI: [10.](https://doi.org/10.5281/zenodo.10102508)
684 [5281/zenodo.10102508](https://doi.org/10.5281/zenodo.10102508). URL: <https://doi.org/10.5281/zenodo.10102508>.
- 685 [40] Man-Fai Ng et al. “Predicting the state of charge and health of batteries using data-driven
686 machine learning”. In: *Nature Machine Intelligence* 2.3 (2020), pp. 161–170. DOI: [10.1038/](https://doi.org/10.1038/s42256-020-0156-7)
687 [s42256-020-0156-7](https://doi.org/10.1038/s42256-020-0156-7).

- [41] Zhaoyang Niu, Guoqiang Zhong, and Hui Yu. “A review on the attention mechanism of deep learning”. In: *Neurocomputing* 452 (2021), pp. 48–62. DOI: [10.1016/j.neucom.2021.03.091](https://doi.org/10.1016/j.neucom.2021.03.091).
- [42] Leah Nuss et al. *Formation and cycling data for Na-ion batteries from high-throughput synthesis, coating, and assembly*. Version v1. May 2023. DOI: [10.5281/zenodo.7981011](https://doi.org/10.5281/zenodo.7981011). URL: <https://doi.org/10.5281/zenodo.7981011>.
- [43] Adam Paszke et al. “PyTorch: An Imperative Style, High-Performance Deep Learning Library”. In: *Advances in Neural Information Processing Systems 32*. Curran Associates, Inc., 2019, pp. 8024–8035. URL: <http://papers.neurips.cc/paper/9015-pytorch-an-imperative-style-high-performance-deep-learning-library.pdf>.
- [44] Lutz Prechelt. “Early stopping-but when?” In: *Neural Networks: Tricks of the trade*. Springer, 2002, pp. 55–69. DOI: [10.1007/978-3-642-35289-8_5](https://doi.org/10.1007/978-3-642-35289-8_5).
- [45] Paul Raccuglia et al. “Machine-learning-assisted materials discovery using failed experiments”. In: *Nature* 533.7601 (2016), pp. 73–76. DOI: [10.1038/nature17439](https://doi.org/10.1038/nature17439).
- [46] Fuzhan Rahmanian et al. “Conductivity experiments for electrolyte formulations and their automated analysis”. In: *Scientific Data* 10.1 (2023), p. 43. DOI: [10.1038/s41597-023-01936-3](https://doi.org/10.1038/s41597-023-01936-3).
- [47] Laura Hannemose Rieger et al. “Uncertainty-aware and explainable machine learning for early prediction of battery degradation trajectory”. In: *Digital Discovery* 2.1 (2023). DOI: [10.1039/D2DD00067A](https://doi.org/10.1039/D2DD00067A).
- [48] Darius Roman et al. “Machine learning pipeline for battery state-of-health estimation”. In: *Nature Machine Intelligence* 3.5 (2021), pp. 447–456. DOI: [10.1038/s42256-021-00312-3](https://doi.org/10.1038/s42256-021-00312-3).
- [49] Jerret Ross et al. “Large-scale chemical language representations capture molecular structure and properties”. In: *Nature Machine Intelligence* 4.12 (2022), pp. 1256–1264. DOI: [10.1038/s42256-022-00580-7](https://doi.org/10.1038/s42256-022-00580-7).
- [50] Bhaskar Saha and Kai Goebel. *NASA Prognostics Data Repository*. 2007. URL: <https://www.nasa.gov/content/prognostics-center-of-excellence-data-set-repository>.
- [51] Kristen A Severson et al. “Data-driven prediction of battery cycle life before capacity degradation”. In: *Nature Energy* 4.5 (2019), pp. 383–391. DOI: [10.1038/s41560-019-0356-8](https://doi.org/10.1038/s41560-019-0356-8).
- [52] AJ Smith et al. “Precision measurements of the coulombic efficiency of lithium-ion batteries and of electrode materials for lithium-ion batteries”. In: *Journal of The Electrochemical Society* 157.2 (2009), A196. DOI: [10.1149/1.3268129](https://doi.org/10.1149/1.3268129).
- [53] Anna Smith et al. “Potential and limitations of research battery cell types for electrochemical data acquisition”. In: *Batteries & Supercaps* 6.6 (2023), e202300080. DOI: [10.1002/batt.202300080](https://doi.org/10.1002/batt.202300080).
- [54] Helge Sören Stein. “Nonlinear potentiodynamic battery charging protocols for fun, education, and application”. In: *ChemRxiv* (2023). DOI: [10.26434/chemrxiv-2023-vj5n0](https://doi.org/10.26434/chemrxiv-2023-vj5n0).
- [55] Calum Strange and Goncalo Dos Reis. “Prediction of future capacity and internal resistance of Li-ion cells from one cycle of input data”. In: *Energy and AI* 5 (2021), p. 100097. DOI: [10.1016/j.egyai.2021.100097](https://doi.org/10.1016/j.egyai.2021.100097).
- [56] Zheming Tong et al. “Early prediction of remaining useful life for Lithium-ion batteries based on a hybrid machine learning method”. In: *Journal of Cleaner Production* 317 (2021), p. 128265. DOI: [10.1016/j.jclepro.2021.128265](https://doi.org/10.1016/j.jclepro.2021.128265).
- [57] Yi Wang et al. “Probabilistic individual load forecasting using pinball loss guided LSTM”. In: *Applied Energy* 235 (2019), pp. 10–20. DOI: [10.1016/j.apenergy.2018.10.078](https://doi.org/10.1016/j.apenergy.2018.10.078).
- [58] Mark D Wilkinson et al. “The FAIR Guiding Principles for scientific data management and stewardship”. In: *Scientific Data* 3.1 (2016), pp. 1–9. DOI: [10.1038/sdata.2016.18](https://doi.org/10.1038/sdata.2016.18).
- [59] Billy Wu et al. “Battery digital twins: Perspectives on the fusion of models, data and artificial intelligence for smart battery management systems”. In: *Energy and AI* 1 (2020), p. 100016. DOI: [10.1016/j.egyai.2020.100016](https://doi.org/10.1016/j.egyai.2020.100016).
- [60] Changwen Xu, Yuyang Wang, and Amir Barati Farimani. “TransPolymer: a Transformer-based language model for polymer property predictions”. In: *npj Computational Materials* 9.1 (2023), p. 64. DOI: [10.1038/s41524-023-01016-5](https://doi.org/10.1038/s41524-023-01016-5).

- 739 [61] Yuzhi Xu, Jiankai Ge, and Cheng-Wei Ju. “Machine learning in energy chemistry: introduction,
740 challenges and perspectives”. In: *Energy Advances* 2.7 (2023), pp. 896–921. DOI: [10.1039/
741 D3YA00057E](https://doi.org/10.1039/D3YA00057E).
- 742 [62] Fangfang Yang et al. “A coulombic efficiency-based model for prognostics and health estimation
743 of lithium-ion batteries”. In: *Energy* 171 (2019), pp. 1173–1182. DOI: [10.1016/j.
744 energy.2019.01.083](https://doi.org/10.1016/j.energy.2019.01.083).
- 745 [63] Yixin Yang. “A machine-learning prediction method of lithium-ion battery life based on charge
746 process for different applications”. In: *Applied Energy* 292 (2021), p. 116897. DOI: [10.1016/j.
747 apenergy.2021.116897](https://doi.org/10.1016/j.apenergy.2021.116897).
- 748 [64] Zhenpeng Yao et al. “Machine learning for a sustainable energy future”. In: *Nature Reviews
749 Materials* 8.3 (2023), pp. 202–215. DOI: [10.1038/s41578-022-00490-5](https://doi.org/10.1038/s41578-022-00490-5).
- 750 [65] Jaekyun Yoo et al. “An artificial neural network using multi-head intermolecular attention for
751 predicting chemical reactivity of organic materials”. In: *Journal of Materials Chemistry A* 11.24
752 (2023), pp. 12784–12792. DOI: [10.1039/D2TA07660H](https://doi.org/10.1039/D2TA07660H).
- 753 [66] Yunwei Zhang et al. “Identifying degradation patterns of lithium ion batteries from impedance
754 spectroscopy using machine learning”. In: *Nature communications* 11.1 (2020), p. 1706. DOI:
755 [10.1038/s41467-020-15235-7](https://doi.org/10.1038/s41467-020-15235-7).
- 756 [67] Zhang et al. *Cycling Data of 64 Cells manufactured by AutoBASS*. Version 2. Nov. 2022. DOI:
757 [10.5281/zenodo.7299473](https://doi.org/10.5281/zenodo.7299473). URL: <https://doi.org/10.5281/zenodo.7299473>.
- 758 [68] Chunxiang Zhu et al. “Prognosis of Lithium-Ion Batteries’ Remaining Useful Life Based on a
759 Sequence-to-Sequence Model with Variational Mode Decomposition”. In: *Energies* 16.2 (2023),
760 p. 803. DOI: [10.3390/en16020803](https://doi.org/10.3390/en16020803).
- 761 [69] Jiangong Zhu et al. *Data-driven capacity estimation of commercial lithium-ion batteries from
762 voltage relaxation*. Apr. 2022. DOI: [10.5281/zenodo.6405084](https://doi.org/10.5281/zenodo.6405084). URL: [https://doi.org/10.
763 5281/zenodo.6405084](https://doi.org/10.5281/zenodo.6405084).
- 764 [70] Jiangong Zhu et al. “Data-driven capacity estimation of commercial lithium-ion batteries from
765 voltage relaxation”. In: *Nature communications* 13.1 (2022), p. 2261. DOI: [10.1038/s41467-
766 022-29837-w](https://doi.org/10.1038/s41467-022-29837-w).